

AD-A195 144

NUMERICAL SIMULATION OF NOZZLE FLOWS(U) RUTGERS - THE
STATE UNIV NEW BRUNSWICK NJ DEPT OF MECHANICAL A.

1/1

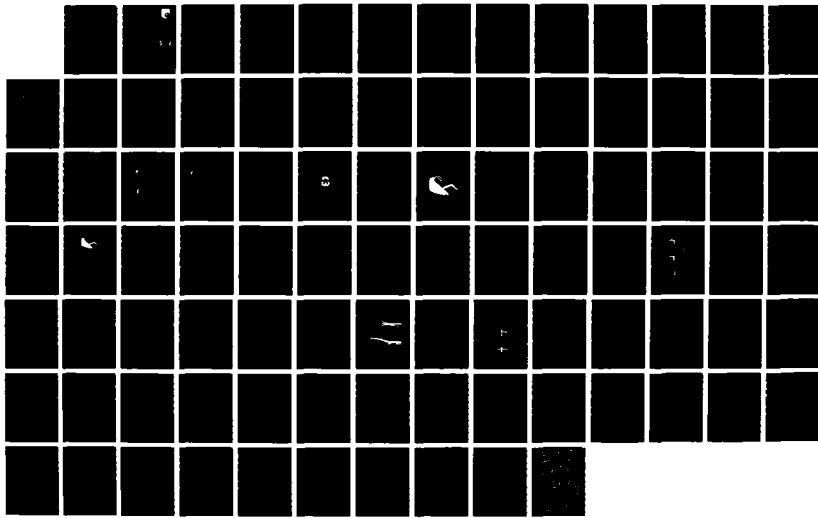
D D KNIGHT ET AL. 18 FEB 89 RU-TR-169-MAE-F

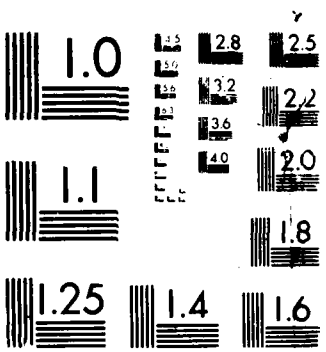
UNCLASSIFIED

AFWAL-TR-87-3110 F33615-84-K-3009

F/G 20/4

NL





MICROFILM RESOLUTION TEST CHART
NATIONAL BUREAU OF STANDARDS 1964

DTIC FILE COPY

(2)

AD-A195 144

AFWAL-TR-87-3110



Numerical Simulation of Nozzle Flows

Doyle D. Knight

Datta V. Gaitonde

Department of Mechanical and Aerospace Engineering

Rutgers University

New Brunswick, New Jersey 08903

18 February 1988

DTIC
SELECTED
MAY 17 1988
S C₉ D **D**

Final Report for Period May 84 - August 87

Approved for public release; distribution unlimited

FLIGHT DYNAMICS LABORATORY
AIR FORCE WRIGHT AERONAUTICAL LABORATORIES
AIR FORCE SYSTEMS COMMAND
AFWAL/FIMM
WRIGHT-PATTERSON AIR FORCE BASE, OHIO 45433-6553

88 5 16 v18

NOTICE

When Government drawings, specifications, or other data are used for any purpose other than in connection with a definitely Government-related procurement, the United States Government incurs no responsibility or any obligation whatsoever. The fact that the Government may have formulated or in any way supplied the said drawings, specifications, or other data, is not to be regarded by implication, or otherwise in any manner construed, as licensing the holder, or any other person or corporation; or as conveying any rights or permission to manufacture, use, or sell any patented invention that may in any way be related thereto.

This report has been reviewed by the Office of Public Affairs (ASD/PA) and is releasable to the National Technical Information Service (NTIS). At NTIS, it will be available to the general public, including foreign nations.

This technical report has been reviewed and is approved for publication.

Kervyn D Mach
KERVYN D. MACH, Aerospace Engr.
Computational Aerodynamics Gr.
Aerodynamics and Airframe Branch

Joseph S Shang
JOSEPH J. S. SHANG, Technical Manager
Computational Aerodynamics Group
Aerodynamics and Airframe Branch
Aeromechanics Division

FOR THE COMMANDER

Alfred C Draper
ALFRED C. DRAPER
Acting Chief
Aeromechanics Division

If your address has changed, if you wish to be removed from our mailing list, or if the addressee is no longer employed by your organization please notify AFWAL/FIMM, Wright-Patterson AFB, OH 45433-6553 to help us maintain a current mailing list.

Copies of this report should not be returned unless return is required by security considerations, contractual obligations, or notice on a specific document.

Unclassified

SECURITY CLASSIFICATION OF THIS PAGE

Form Approved
OMB No. 0704-0188

REPORT DOCUMENTATION PAGE					
1a. REPORT SECURITY CLASSIFICATION Unclassified		1b. RESTRICTIVE MARKINGS			
2a. SECURITY CLASSIFICATION AUTHORITY		3. DISTRIBUTION/AVAILABILITY OF REPORT Approved for public release; distribution is unlimited.			
2b. DECLASSIFICATION/DOWNGRADING SCHEDULE					
4. PERFORMING ORGANIZATION REPORT NUMBER(S) RU-TR-169-MAE-F		5. MONITORING ORGANIZATION REPORT NUMBER(S) AFWAL-TR-87-3110			
6a. NAME OF PERFORMING ORGANIZATION Dept of Mech. and Aero. Engr. Rutgers University	6b. OFFICE SYMBOL (If applicable) MAE	7a. NAME OF MONITORING ORGANIZATION Flight Dynamics Laboratory (AFWAL/FIMM) Air Force Wright Aeronautical Laboratories			
6c. ADDRESS (City, State, and ZIP Code) Dept of Mech & Aero Engr Rutgers University, P.O. Box 909 Piscataway NJ 08855-0909		7b. ADDRESS (City, State, and ZIP Code) Wright-Patterson AFB OH 45433-6553			
8a. NAME OF FUNDING/SPONSORING ORGANIZATION Flight Dynamics Laboratory	8b. OFFICE SYMBOL (If applicable) AFWAL/FIMM	9. PROCUREMENT INSTRUMENT IDENTIFICATION NUMBER F33615-84-K-3009			
8c. ADDRESS (City, State, and ZIP Code) Wright-Patterson AFB OH 45433-6553		10. SOURCE OF FUNDING NUMBERS			
		PROGRAM ELEMENT NO 61102F	PROJECT NO 2307	TASK NO N6	WORK UNIT ACCESSION NO. 10
11. TITLE (Include Security Classification) NUMERICAL SIMULATION OF NOZZLE FLOWS					
12. PERSONAL AUTHOR(S) Doyle Knight and Datta Gaitonde					
13a. TYPE OF REPORT Final	13b. TIME COVERED FROM May 84 to Aug 87	14. DATE OF REPORT (Year, Month, Day) 18 February 1988		15. PAGE COUNT 88	
16. SUPPLEMENTARY NOTATION Three-dimensional finite difference, -					
17. COSATI CODES		18. SUBJECT TERMS (Continue on reverse if necessary and identify by block number) Nozzle Flows; Viscous-Inviscid Interactions; Computational Fluid Dynamics; Navier-Stokes Equations; Turbulence .			
19. ABSTRACT (Continue on reverse if necessary and identify by block number) A three-dimensional grid generation code implementing the Multisurface technique is developed with major emphasis on the use of color computer graphics. A precise control method is employed to permit grid point control. A significant departure from existing approaches is the extension of user interaction to all phases of grid generation. This facilitates easy and rapid developments of grids especially for 3-D applications. The code is employed to generate grids for a 3-D axisymmetric nozzle and an aircraft type section. The flow in a non-axisymmetric nozzle is computed under the assumptions of horizontal and vertical symmetry. The Mach number of external flow is 1.2. The results are validated by comparison with experiment. Overall good agreement is observed with static pressure comparisons. Preliminary flow analysis indicates the existence of a number of interesting flow structures including shocks, pressure wave systems and regions of flow separation.					
20. DISTRIBUTION/AVAILABILITY OF ABSTRACT <input checked="" type="checkbox"/> UNCLASSIFIED/UNLIMITED <input type="checkbox"/> SAME AS RPT <input type="checkbox"/> DTIC USERS			21. ABSTRACT SECURITY CLASSIFICATION UNCLASSIFIED		
22a. NAME OF RESPONSIBLE INDIVIDUAL K. Mach			22b. TELEPHONE (Include Area Code) (513) 255-2455	22c. OFFICE SYMBOL AFWAL/FIMM	

Table of Contents

1. Introduction	1
2. Three-Dimensional Interactive Grid Generation Using the Multisurface Technique	4
2.1. Introduction	4
2.2. Grid Requirements	7
2.3. Phase I: Grid Generation by Multisurface Interpolation	7
2.4. Phase II: Direct Grid Modification	10
2.5. Description of Code	12
2.6. Applications	14
2.7. Conclusion	19
3. Simulation of Nozzle Flows	25
3.1. Introduction	25
3.2. Brief Description of Experiments	27
3.3. Topological Discussion	27
3.4. Theoretical Model	39
3.5. Numerical Algorithm	43
3.6. Details of Implementation of Eddy Viscosity	45
3.7. Coordinate Transformation and Geometrical Simplifications	47
3.8. Initial and Boundary Conditions	54
3.9. Computational Details	59
3.10. Comparison with Experiment	63
3.11. Analysis of Computed Flow Field Structure	65
3.12. Conclusion	69
4. Conclusion and Future Work	72
References	74
Nomenclature	80

Accession For	
NTIS	CRA&I <input checked="" type="checkbox"/>
DTIC	TAB <input type="checkbox"/>
Unannounced <input type="checkbox"/>	
Justification _____	
By _____	
Distribution /	
Availability Classes	
Print	1st Copy and/or Serial
A-1	



List of Figures

Figure 2-1: Curvilinear Grids - Physical and Transformed Planes	5
Figure 2-2: Grid Generation Approach of this Research	6
Figure 2-3: Twin-Jet Axisymmetric Nozzle	8
Figure 2-4: The Multisurface Technique	9
Figure 2-5: Precise Point Distribution Control	11
Figure 2-6: Grid Configuration at Axial Station for Twinjet Nozzle	15
Figure 2-7: Transformed Plane for Twinjet Nozzle	16
Figure 2-8: Sub-Zones at Typical Twinjet Nozzle Section	17
Figure 2-9: Intermediate and Bounding Surface Description for Twinjet Nozzle	18
Figure 2-10: Intermediate Surfaces for Zones 1 and 2	20
Figure 2-11: Subgrids at Section Upstream of Nozzle Exit	21
Figure 2-12: Composite Grid at Section Upstream of Nozzle Exit	22
Figure 2-13: Schematic of Aircraft Section Grid	22
Figure 2-14: Intermediate Surface Structure for Aircraft Section	23
Figure 2-15: Final Grid for Aircraft Section	24
Figure 3-1: Non-Axisymmetric Nozzle In Low-Expansion Configuration. From [46]	26
Figure 3-2: Air-Powered Nacelle Model with Nonaxisymmetric Plug Nozzle Installed. From [46]	28
Figure 3-3: Internal and External Geometry. From [46]	30
Figure 3-4: General Flow Structure - Top and Side Views	33
Figure 3-5: Physical and Transformed Domains - Nonaxisymmetric Nozzle	34
Figure 3-6: General Physical and Corresponding Transformed Plane	36
Figure 3-7: Different Types of Cross Sections	37
Figure 3-8: Ordinary and Sublayer Regions	44
Figure 3-9: Implementation of Eddy Viscosity Model Near Internal Corner	46
Figure 3-10: Implementation of Eddy Viscosity in Region 7	50
Figure 3-11: Interfacing of Eddy Viscosity Models at Type III Cross Section	51
Figure 3-12: Modification of Wedge Leading Edge	52
Figure 3-13: Grids in $j = \text{constant}$ planes	53
Figure 3-14: Grids in $i = \text{constant}$ planes	55
Figure 3-15: Modification at Trailing Edge of Flap	56
Figure 3-16: Boundary Conditions at Each Type of Section	60
Figure 3-17: Computation of Transverse Pressure Gradient In Sublayer at External Corner	62
Figure 3-18: Location of Experimental Static Pressure Orifices. From [46]	64
Figure 3-19: Static Pressure Variation on Wedge Centerline - Comparison with Experiment	66
Figure 3-20: Static Pressure Variation on Flap Inner Centerline - Comparison with Experiment	67
Figure 3-21: Static Pressure Variation on Flap Outer Centerline - Comparison with Experiment	68

Figure 3-22: Development of Static Pressure at Upstream Internal Flow Boundary 70

Figure 3-23: Static Pressure Near Sidewall-Wedge Corner 71

List of Tables

Table 3-1: Flow Conditions In Experiment	29
Table 3-2: Boundary Layer Thicknesses	48
Table 3-3: X-locations (cm.)	54
Table 3-4: Summary of Static Pressure Orifice Locations	65

Acknowledgements

The authors would like to acknowledge the assistance of Dr. Joseph Shang and K. Mach of the Air Force Wright Aeronautical Laboratories, Wright-Patterson AFB, Ohio. The support of the staff of the John von Neumann Supercomputer Center, where all computations were carried out, is also gratefully noted.

1. Introduction

The present and anticipated roles of tactical aircraft impose serious challenges for the design of aircraft exhaust nozzles. Present or expected aircraft requirements include decreased aftbody drag through improved airframe-propulsion integration, enhanced aircraft maneuver capability, short take-off and landing (STOL), reduced aircraft observables and increased supersonic cruise range ([1]- [6]).

The accurate prediction of the performance of exhaust nozzle flows is challenging due to several factors, including:

- Strong viscous-inviscid interaction: Flow separation in the vicinity of the exhaust nozzle(s) is a common characteristic, due to strong shock-boundary layer interaction or adverse pressure gradients in the absence of shocks ([7]- [10]).
- Complicated geometrical shapes: The integration of exhaust nozzles into the airframe results in non-simple three dimensional geometrical shapes which can generate complex 3-D flow patterns. For example, the integration of twin-jet axisymmetric nozzles with a rectangular fuselage is sometimes achieved through the use of boattailed "gutter" interfairings, which can adversely affect vehicle drag [11].
- Unsteady flow fields: The geometry of certain exhaust nozzle-airframe integrations is possibly subject to low frequency unsteady fluid motion. For example, the region between two widely-separated twin-jet axisymmetric nozzles may be analogous to an "open" cavity, which are observed to display self-sustained oscillations in a number of different geometrical configurations ([12]- [15]).

The current approach to the design and evaluation of exhaust nozzles relies heavily on sub- and full-scale model tests and empirical correlations ([2], [4]- [8], [16]- [18]). Theoretical analysis typically consists of a combined inviscid-boundary layer approach, with empirical corrections to account for the discrepancy between prediction and experiment [6]. This method, however, is incapable of handling strong viscous-inviscid interactions, and has failed to accurately predict the performance of some advanced nozzle

configurations [6]. The evolution towards improved airframe-propulsion integration and the increased geometric complexity in nozzle designs (e.g., single expansion ramp nozzle [SERN], 2-D converging-diverging [C/D] nozzles with yaw and pitch vectoring) results in a dramatic increase in the number of configurations to be tested, and an associated rise in development costs.

In recent years, the capability for accurate and efficient numerical simulation of complex flows involving strong viscous-inviscid interactions has been significantly enhanced by two factors. First, the advent of modern high-speed vector-processing computers (such as the CRAY-XMP and CYBER 205) has afforded typically one to two orders of magnitude improvement [19, 20, 21, 22] in computational efficiency compared to the earlier generation computers such as the CDC 6600 and IBM 370/168. Second, the development of efficient implicit and hybrid implicit-explicit numerical algorithms for the full unsteady mean (Reynolds-averaged) Navier-Stokes equations ([21], [23]-[27]) has also enhanced computational efficiency. As a consequence, emerging design methodologies for exhaust nozzles, as well as other aircraft components, envision the utilization of full Navier-Stokes numerical simulations as part of a hierarchy of theoretical approaches which also include the traditional combined inviscid-boundary layer analysis and the recently developed parabolized Navier-Stokes methods [28]. Together, these approaches can be combined with experimental testing in order to minimize the number of configurations in the required experimental test matrix [29], thereby allowing greater attention to a selected number of experimental test configurations, and a reduction in overall development costs.

A number of steady 2-D/axisymmetric numerical simulations of nozzle exhaust flow fields have been performed in recent years using the compressible Navier-Stokes equations. These include the computations of axisymmetric nozzles by Mikhail, Hankey and Shang [30] and Hasen [31], and two-dimensional nozzles by Cline and Wilmoth [32] and Perry [33]. Steady three-dimensional exhaust nozzle computations have been performed using the mean Navier-Stokes equations. However, unsteady two-dimensional compressible laminar Navier-Stokes calculations have been performed for spike-tipped

bodies by Shang, Smith and Hankey [15] and for flow past a cylinder by Shang [34]. In addition, unsteady 2-D turbulent Navier-Stokes simulations have been computed by Levy [35] for a circular arc transonic airfoil, and by Steger and Bailey [20] for the transonic flow past the F-80 wing. In these latter cases, the unsteady flow was characterized by low frequency motion (time scales on the order of the mean flow), and the effects of the high frequency turbulent motion was incorporated through an algebraic turbulent eddy viscosity model.

The primary objective of this research is to develop and evaluate the ability to simulate complex nozzle flows. The solution of problems with finite difference methods (CFD) consists of three major phases: mesh generation, flow computation and flow analysis. The complex geometries encountered in nozzle flows consist of curved or irregularly shaped boundaries for which grid generation becomes a task in itself. Uniformly discretized grids in the physical domain are inadequate since in addition to difficulties encountered in application of boundary conditions, the accuracy of the computation may be affected and it may be impossible to achieve adequate resolution in regions with large gradients with a limited number of mesh points. A number of techniques of grid generation for finite difference applications are summarized in [36] and [37]. From a survey of the literature, though a number of techniques have been proposed for 3-D grid generation, evidently the focus of application has been on 2-D cases. A need further exists to incorporate interactive graphics [38] into the grid generation process to reduce the time required to generate complex grids. This report describes the implementation of one particular method (the multisurface technique of Eiseman [39]).

The focus of the nozzle flow simulation is on steady flow in a nonaxisymmetric wedge nozzle at a freestream Mach number of 1.2. The choice of this case is dictated by the existence of experimental investigations with surface pressure measurements (subsection 3.2). The explicit-implicit algorithm employed (subsections 3.4 and 3.5) is applicable for axisymmetric nozzles as well, although some additional work may be necessary, however, to resolve coordinate transformation singularities.

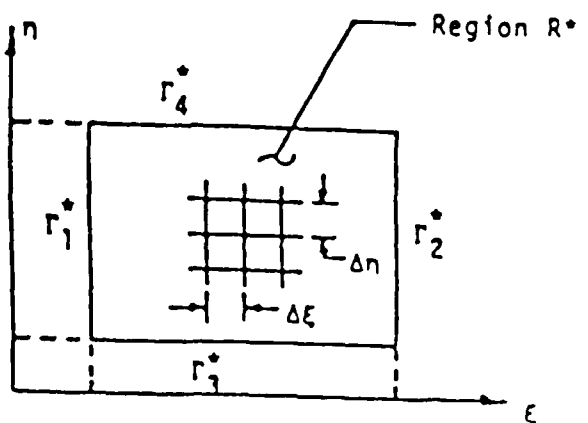
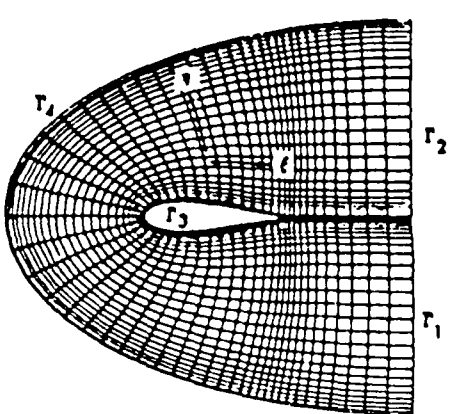
The application of the multi-surface technique of Eiseman is described in Section 2. Section 3 describes the nozzle flow computation including the theoretical model for nozzle flow (governing equations and turbulence model), grid details and preliminary numerical results. Section 4 concludes with some remarks on the current ability to simulate nozzle flows and identifies areas of future work.

2. Three-Dimensional Interactive Grid Generation Using the Multisurface Technique

2.1. Introduction

The use of body-fitted grids considerably simplifies the problem of flow simulation using finite difference techniques in domains with curved boundaries. For such domains, the employment of Cartesian and other standard meshes becomes cumbersome since interpolation is generally necessary at the boundaries. It is also difficult if not impossible to concentrate the grid in arbitrary regions of space without introducing a large number of unnecessary mesh points [40]. The basic concept is to map the given complicated physical domain and the governing equations into a topologically simpler domain as shown in Fig. 2-1, which demonstrates the procedure for flow about an airfoil. A significant amount of effort has been focussed recently on the development of adequate grid generation techniques applicable to general geometries. Ref. [41] provides an overview of this effort.

The standard approach to grid generation involves the application of a selected grid generation algorithm (e.g., the multisurface technique of Eiseman [39]) to a specific configuration. The algorithm may utilize one or more techniques for grid point distribution (e.g., the location of intermediate surfaces in the algebraic grid generation method of Eiseman [39]). The grid is subsequently examined for satisfaction of the specified grid requirements (e.g., orthogonality of the grid lines near solid boundaries). If the grid is deemed unsatisfactory, the input to the grid generation algorithm is modified (e.g., the location of the intermediate surfaces), and the grid recomputed. This process of grid generation, diagnosis, and modification of input variables is continued until a satisfactory



$$\begin{aligned}\eta &= \eta(x, y) \\ \xi &= \xi(x, y)\end{aligned}$$

$$\begin{aligned}x &= x(\eta, \xi) \\ y &= y(\eta, \xi)\end{aligned}$$

Figure 2-1: Curvilinear Grids - Physical and Transformed Planes

grid is achieved.

The specific grid requirements of a given application, however, may not be completely or easily met by the above approach. In the current research effort, a two-phase methodology is developed (Fig. 2-2). Phase I employs a grid generation algorithm (the multisurface technique of Eiseman [39]) and an algorithm for control of grid point distribution (the method of Smith *et al*[42]). The purpose of the first phase (Phase I) is to obtain an approximate grid satisfying part of the grid requirements. Phase II employs graphical techniques to *directly* modify local areas of the grid to meet the remaining grid requirements. The second phase is performed independently of, and subsequent to, the grid generation by the specified algorithm (Phase I). Both phases are incorporated in an interactive environment utilizing color graphics.

It is evident from a survey of the literature that while significant effort has been focussed on the generation of 2-D grids, there have been relatively fewer applications of 3-D

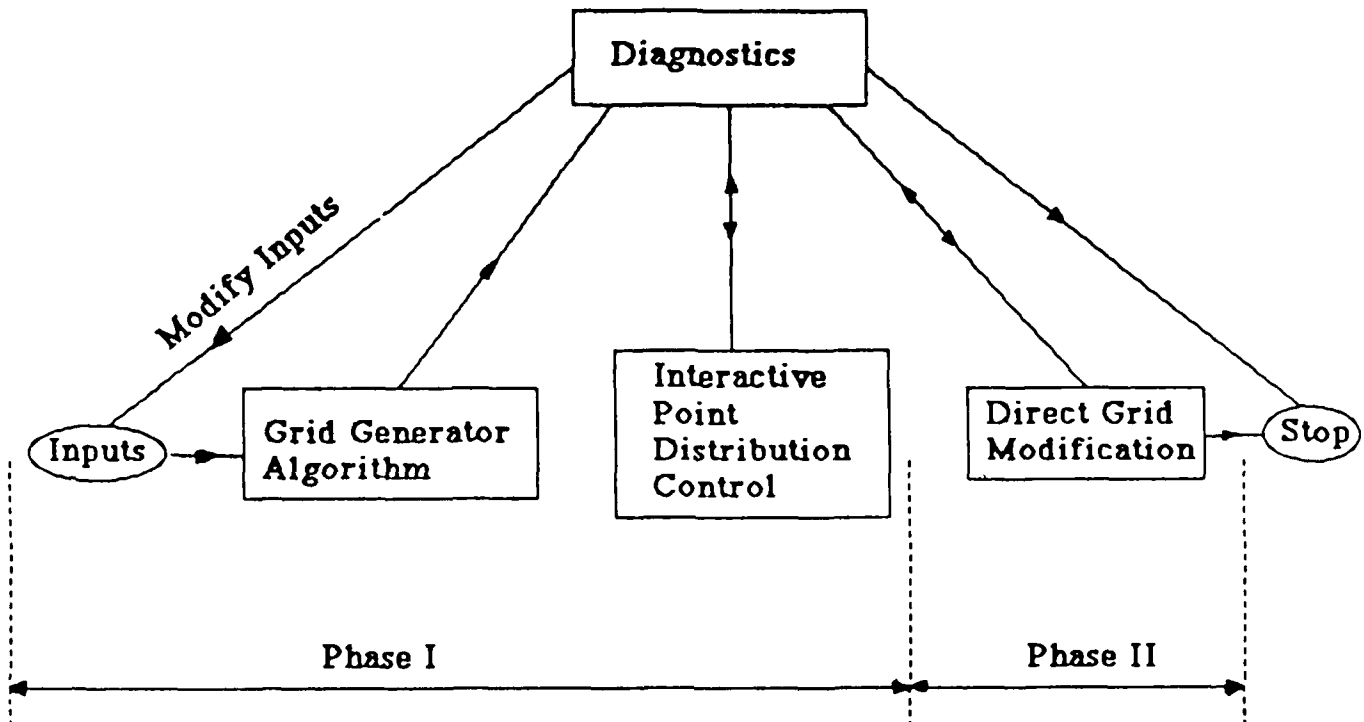


Figure 2-2: Grid Generation Approach of this Research

methods. This is because the volume and visual complexity of data specification increases significantly making the use of interactive graphics (in particular analog graphical input) imperative. While the importance of graphics for evaluation of generated grids has long been recognized, the applicability of interactive graphics techniques in the grid generation phase itself has not been extensively explored (with the notable exception of the work of Smith *et al*[42]).

This section describes a three-dimensional graphics-based interactive grid generation program. The use of graphics is extended to all stages of grid generation with particular emphasis on direct modification. The code has the capability of generating meshes for general configurations. Two typical examples are presented.

2.2. Grid Requirements

While the intent of this research is to develop a method with broad application, for concreteness the twin-jet axisymmetric nozzle is considered (see Fig. 2-3). This configuration displays several of the principal features related to grid topologies of practical interest. These are summarized as follows:

- Body shape exhibits transition in shape
- Two flows, inner and outer, which meet at the nozzle exit exist. The mixing of these constitutes the wake region which must be resolved with an adequate grid.

In addition to these, the numerical algorithm employed in the solution of the flow equations introduces some constraints. We arrived at the following general constraints by considering a number of algorithms - the explicit method of McCormack [43], the hybrid explicit-implicit method of Knight [44] and the implicit method of Beam and Warming [25].

- Orthogonality is desirable in boundary layer regions, especially for implementation of algebraic eddy viscosity models.
- Precise point distribution control is necessary to resolve viscous regions of the boundary layer and the inviscid regions outside the boundary layer.

To simplify the graphical input requirements, the grids are generated in axis-normal sections and stacked together. The control method described below is employed to transmit point distribution information in the axial direction to prevent excessive skewing of grid lines.

2.3. Phase I: Grid Generation by Multisurface Interpolation

The Phase I grid is generated by applying the multisurface technique algorithm described by Eiseman in [39]. In this method, a number of parameterized surfaces are introduced as shown in Fig. 2-4. The basic formula [39] is :

$$P(r,\bar{T}) = P_1(\bar{T}) + \sum_{k=1}^{N-1} A_k G_k(r)[P_{k+1}(\bar{T}) - P_k(\bar{T})] \quad (1)$$

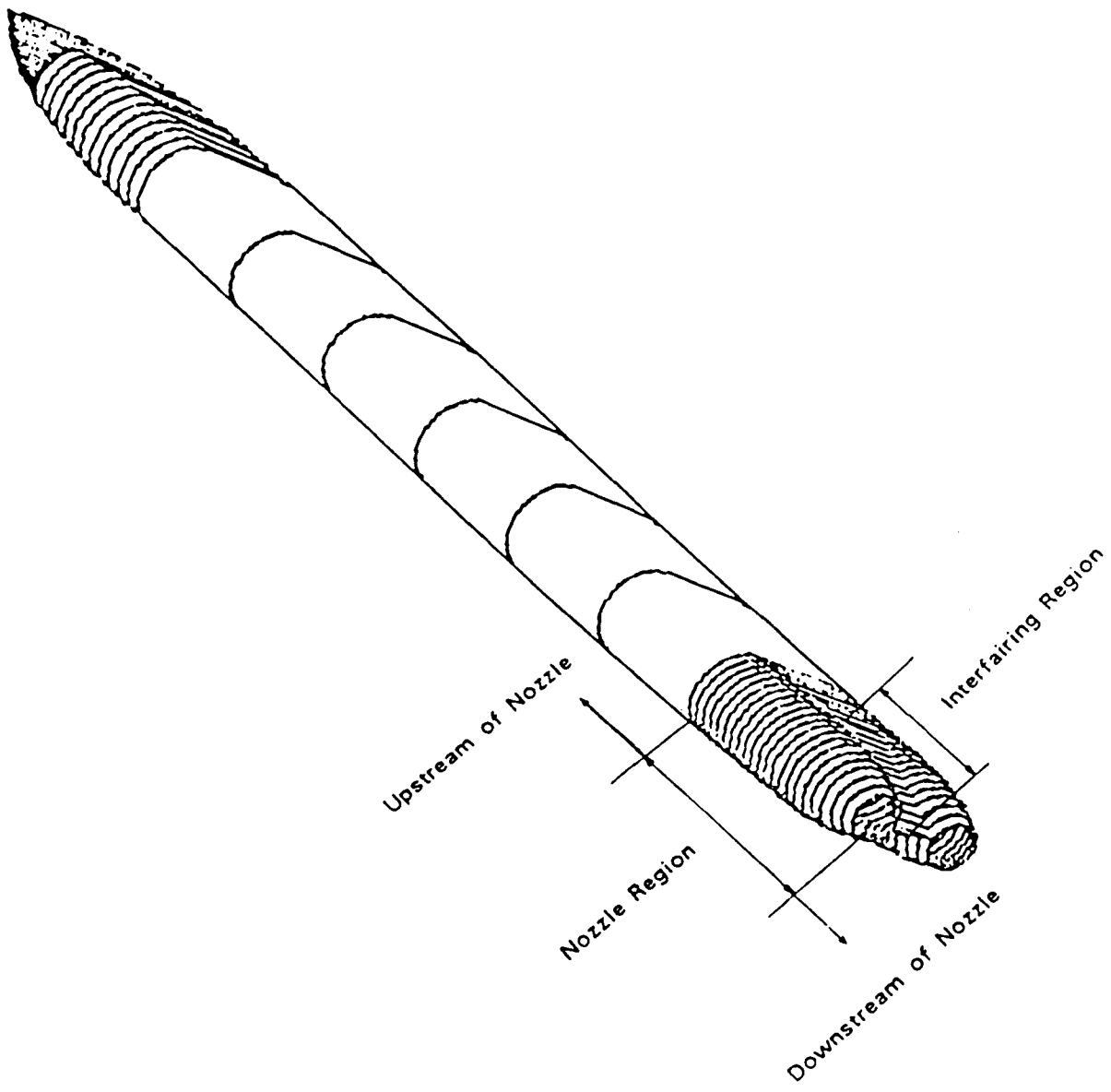


Figure 2-3: Twin-Jet Axisymmetric Nozzle

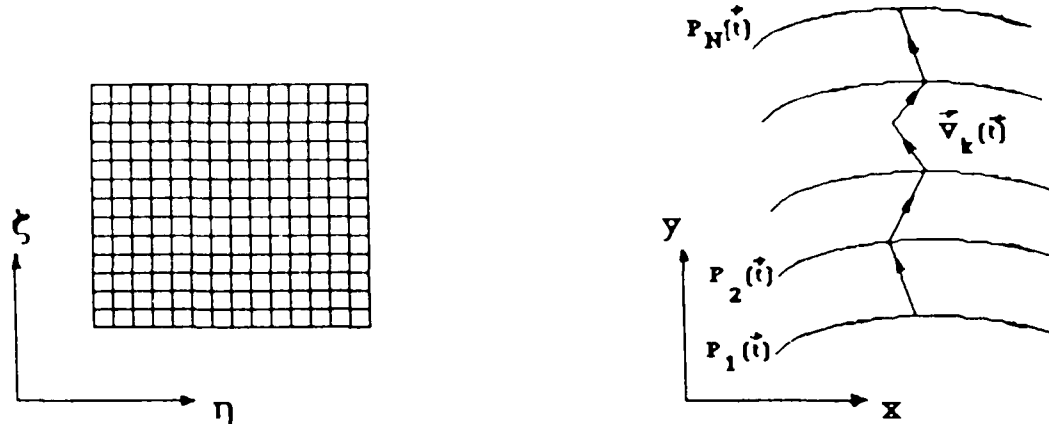


Figure 2-4: The Multisurface Technique

where

$$G_k(r) = \int_{r_1}^r \psi_k(x) dx, \quad (2)$$

and

$$A_k = 1/G_k(r_{N-1}) \quad (3)$$

P_1 through P_N are the parameterized surfaces (with common parameter t), r is the spanning variable (takes the values r_1 and r_{N-1} at the inner and outer bounding surfaces respectively), the functions ψ are interpolants. Choosing A_k as in equation 3 leads to the bounding surfaces being part of the transformation. Depending upon the choice of function for ψ_k , two types of interpolation - global and local may be specified employing respectively globally defined polynomials in r and piecewise linear functions non-vanishing only in a local region. Both methods are incorporated in the current research.

Since precise grid point control through iterative specification of the intermediate surfaces tends to be tedious even in an interactive environment, the control method of Smith et al [42] is employed. This control method provides non-uniform discretization of any general physical variable in a convenient interactive graphical environment. A few points are first digitized on a plot whose ordinate is a parametric variable from the physical

plane and whose abscissa is a normalized variable from the computational plane. A smooth cubic spline is then passed through these points. Shallower regions along this curve correspond to higher concentration of the physical variable discretization.

An example of the application of the control method in this research is shown in Fig. 2-5. The first step in the control of the point distribution in Fig. 2-5(a) is to plot the cumulative arc length profile (CALP) along a cubic spline through the set of points against point number (curve marked "initial" in Fig. 2-5(b)). A new CALP (marked "final") is then digitized or specified analytically. In the present case, the exponential formula :

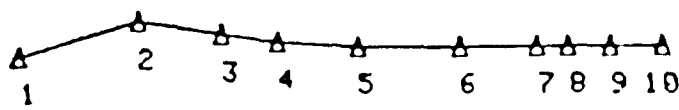
$$\bar{r} = \frac{e^{kr} - 1}{e^k - 1}; \quad 0 \leq r \leq 1 \quad (4)$$

is employed [39] with a k value of 1.0. The new CALP may also be specified to be similar to CALPs of other distributions. The cubic spline coefficients associated with the set of points in Fig. 2-5(a) are then used in conjunction with the new CALP to obtain the new point distribution shown in Fig. 2-5(c). Note that since the "final" curve in Fig. 2-5(b) has a smaller value of slope near point 1, the final distribution has a correspondingly higher concentration near point 1.

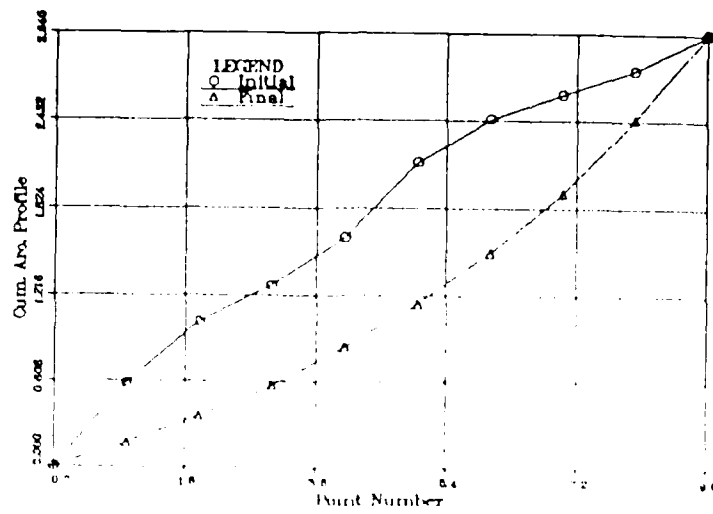
2.4. Phase II: Direct Grid Modification

This phase incorporates a series of powerful graphics based options that facilitate grid modification influencing either the entire grid or only points along a specific grid line. This phase is particularly useful in obtaining special local grid characteristics (e.g., corners) without adversely affecting the entire grid (see subsection 2.6). For example, since the multisurface technique guarantees only that the bounding surfaces are part of the transformation, it is necessary to employ special techniques to obtain precise transverse boundary shapes (e.g., the extreme $\eta = \text{constant}$ lines in Fig. 2-4 in the physical domain)

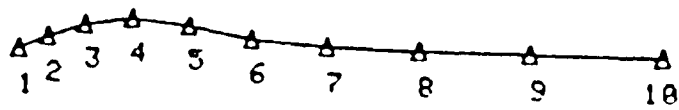
The application of Phase II generally begins with the identification of a set of points along a grid line. The points may be relocated in a variety of ways. Some important options



(a) Initial Point Distribution



(b) Control Plane



(c) Final Point Distribution

Figure 2-5: Precise Point Distribution Control

are :

- Rotation: The points may be rotated about any axis perpendicular to the plane of the grid. The point of intersection between the axis and the plane may be specified either by digitizer or by keyboard input. When the entire grid is identified, as opposed to a set of points along a grid line, rotation may be affected about an arbitrary axis in three-dimensional space. This permits rapid generation of grids for solids of revolution. Reflection about any axis may be achieved by a 180^0 rotation about the appropriate axis.
- Horizontal or vertical alignment: All identified points may be aligned either vertically or horizontally. The use of this option is illustrated later for the twinjet nozzle case.
- Modification with cubic splines: The identified points may be redistributed with the process described earlier in Fig. 2-5.
- Point position modification: Each point may be relocated with graphical or alphanumeric input.
- Change in total number of points: The total number of points in either direction may be increased or reduced without affecting the relative concentration characteristics. This is done by first computing the cubic spline coefficients and CALP for each grid line and inverting the CALP at the new number of grid points to obtain the new grid point distribution

2.5. Description of Code

The three-dimensional graphics-based code is written in Fortran 77 and utilizes graphics device driver routines specific to the Tektronix 41XX series from the Tektronix Interactive Graphics Library (IGL). The program is implemented on a Prime 9955 computer. Input to the code is provided interactively in either a digital (keyboard) or analog (graphics cursor) fashion. Analog input permits the specification of points in physical coordinates such as necessary to define intermediate surfaces and CALPs, identify grid points for direct processing and window areas for visual diagnostics. The sequence of execution of the various modules may be determined by the user. This is called the "command driven" execution mode and provides significant flexibility in the grid generation process. Complete

details of the code are provided in [45].

The grid generation code is split into five modules. These are : surface definition, phase I grid generation, phase II grid generation, diagnostics and grid structuring.

(a) Surface definition: This is generally the first step of the grid generation process and results in the definition on a set of surfaces (inner, outer and intermediate). The surfaces may be defined interactively in one of a number of ways such as through the "joy disk" digitizer, disk files, use of standard ("superellipse") profiles, normals to any previously defined surfaces or on rays passing through corresponding points of a pair of surfaces. It is also possible to introduce point singularities. Once the shape of the surface is defined, the point distribution on these surfaces may be adjusted with the control method described earlier.

(b) Phase I grid generation: In this module, the formulas of subsection 2.3 are employed to generate an initial grid. The spanning variable r may be discretized in a non-uniform fashion using the control plane. This is not effective means of control. In the applications to be described, a uniform discretization is employed.

(c) Phase II grid modification: This module implements the options outlined in subsection 2.4.

(d) Diagnostics: A number of interactive diagnostic measures are incorporated. These include window options which permit detailed telescopic examination of the grid. Two quantities indicative of grid structure, the Jacobian and Skewness measure may also be monitored. The skewness measure (SM) is defined as :

$$SM = \frac{1}{k} \sum_{i=1}^k |90^\circ - \theta_i| \quad (5)$$

where k is the number of angles surrounding a point and the θ_i are the angles measured in degrees.

(e) Grid structuring: This is generally the last executed module. At any given section,

grids may be generated in more than one zone. These zones are combined to form a composite grid through the grid structuring process.

The code generates grids meeting all the requirements outlined in subsection 2.2. The physical features of most geometries of interest are adequately treated with the above surface definition techniques. Orthogonality at the boundary is achieved by defining the first intermediate surface along normals to the inner boundary. Precise point distributions are obtained with the control method of subsection 2.3.

The general strategy is to define intermediate surfaces to satisfy ζ grid line shape and point distribution and η line shape alone to obtain an initial grid (see Fig. 2-4). The graphics based *a posteriori* modification technique (Phase II) is then employed to obtain the precise required distribution along the η lines. The locations of the numerous stacked sections control grid concentration in the remaining third direction.

2.6. Applications

Two applications, chosen to display the versatility of the method, are illustrated. The first case is the twinjet axisymmetric nozzle (Fig. 2-3), while the second represents an aircraft section with an underbelly inlet. In both applications, though grids were generated with both global and local interpolation formulas, only those generated with local interpolation are discussed since they possess superior boundary orthogonality characteristics. Only a few representative grids are shown with the understanding that the characteristics may be altered using the methods outlined earlier. Details of the diagnostic phase are excluded for the purpose of brevity.

(a) Twin-jet axisymmetric nozzle: The general case is a twin-jet nozzle with an interfairing whose trailing edge is of finite thickness and located upstream of the nozzle exit plane. The general grid configuration at an axial station upstream of the nozzle is shown in Fig. 2-6. An appropriate topological plane is shown in Fig. 2-7. Since the shaded areas represent solid regions, no flow computations need be performed here. Note that the entire line AOUNM maps on to the center of the nozzle and as such this represents a singularity

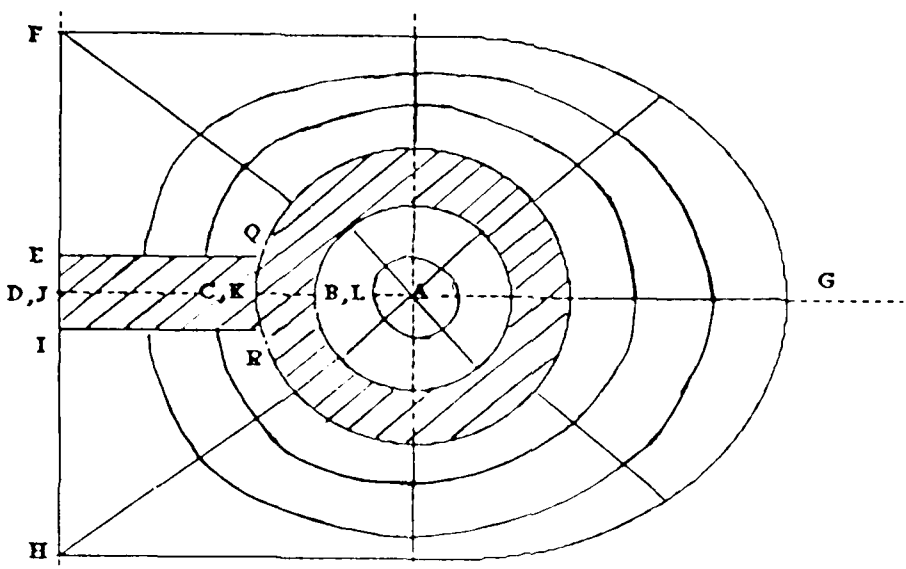


Figure 2-6: Grid Configuration at Axial Station for Twinjet Nozzle

of the transformation. Assuming zero nozzle thickness and vertical and horizontal symmetry, at any section the grid is generated in three sub-zones (Fig. 2-8). Zone 1 representing internal flow region, Zone 2 the external flow region and Zone 3 the interfairing region. Under the assumption that the interfairing trailing edge thickness is zero, Zone 3 is non-critical. However, in the case where the interfairing trailing edge has finite thickness, the grid in this region is important near the trailing edge since it merges with the grids in Zones 1 and 2 to form the wake region. Furthermore, Zone 3 has common adjacent boundaries with Zones 1 and 2 where point distributions must match.

The intermediate surface set for each of these zones is shown in Fig. 2-9. For Zone 1, the inner bounding surface is a point singularity (Point A) corresponding to the center of the nozzle. Note that the flow solution algorithm must take this factor into account. The outer bounding surface is a part of the nozzle surface. One circular intermediate surface (XY) is employed. For Zone 2, the inner bounding surface is the same as the outer surface of Zone 1. Two intermediate surfaces are employed as shown. The outer boundary (EFG)

Upstream of Interfairing Trailing Edge

Transformed Plane

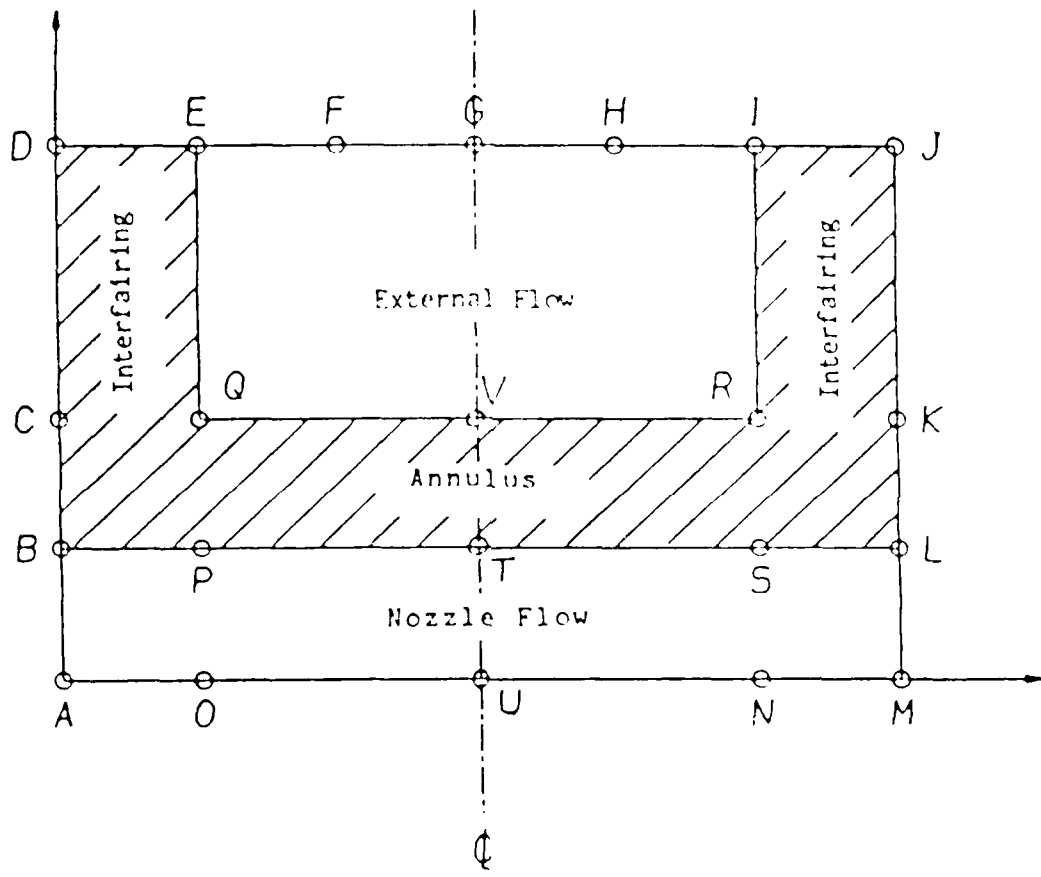


Figure 2-7: Transformed Plane for Twinjet Nozzle

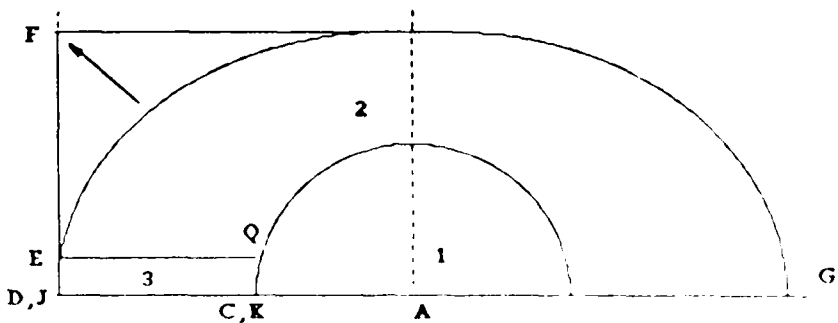
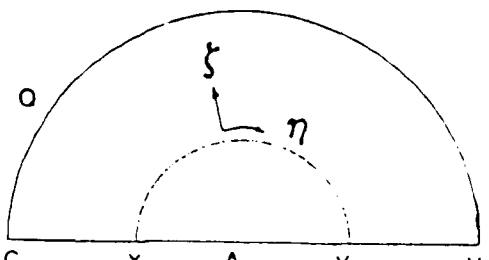


Figure 2-8: Sub-Zones at Typical Twinjet Nozzle Section

has a vertical segment (EF) to facilitate application of symmetry boundary conditions there. If the surface EFG is directly employed in the multisurface technique, the slope discontinuity propagates into the field. This is an undesirable situation since it may adversely affect the flow computation. In this case, the multisurface technique is actually employed with a fictitious elliptic outer surface (see Fig. 2-8) which is later stretched out. This is a typical example where the application of the horizontal or vertical alignment option (Phase II) is useful (see subsection 2.4). Zone 3 is a special zone since the grid point distributions along two adjacent sides (QC and EQ) are known from Zones 1 and 2 respectively. The third boundary ED must be vertical to conform to the vertical line of symmetry. The ordinates of the points along this line are chosen to be identical to those for curve QC and the grid is generated by simple algebraic linear interpolation. There are no intermediate surfaces for this zone and the multisurface technique is never applied.

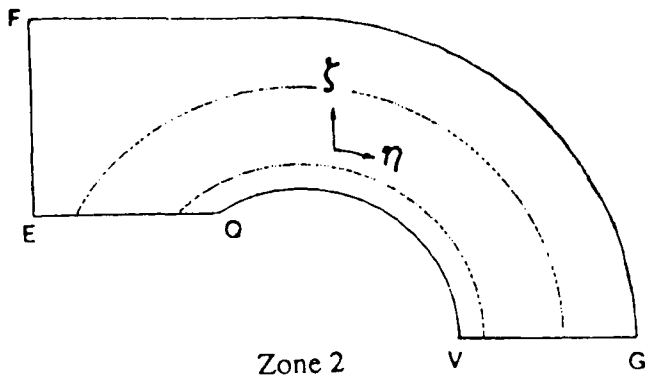
The actual intermediate surface distributions for Zones 1 and 2 are shown in Fig. 2-10. Fig. 2-11 displays the subgrids and Fig. 2-12 shows the final composite grid obtained by structuring the grid sections of Fig. 2-11. All grids are exponentially smoothed towards their respective inner boundaries (see equation <4>). Other distributions may be rapidly generated with the precise control method described earlier. Grids for other sections



Zone 1

Inner boundary: Singularity corresponding to center of nozzle (A).
Outer boundary: Nozzle Surface (CQV).

Intermediate Surfaces (1): Circular (XY).
Points: 20 in eta direction.
15 in zeta direction.



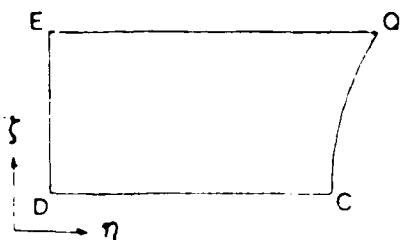
Zone 2

Inner boundary: Nozzle surface (QV).

Outer boundary: Fictitious ellipse (EG).

Intermediate Surfaces (2): Along normals and midway between inner and outer respectively.

Points: 15 in eta direction
20 in zeta direction



Zone 3

Three side distributions known:

EQ - from Zone 2.

QC - from Zone 1.

ED - from QC.

No intermediate surfaces.

Figure 2-9: Intermediate and Bounding Surface Description for Twinjet Nozzle

upstream and downstream of the nozzle exit may be generated in a similar fashion.

(b) Aircraft section with underbelly inlet: The grid for this configuration is generated in five zones shown in Fig. 2-13. The proportions employed are chosen to retain the relevant generic features of such a cross section. Zones 1 through 4 represent regions of external flow. Zones 2 and 3 are reflections of Zones 1 and 4 respectively about a vertical axis. Zone 5 corresponds to the inlet region at any section. Fig. 2-14 displays the intermediate surface set for each zone. The transverse boundaries ABC and FBC are made to confirm precisely to the solid boundary with Phase II techniques discussed in subsection 2.4. Fig. 2-15 shows the exponentially smoothed final grid.

2.7. Conclusion

A 3-D grid generation code, based on the multi-surface technique of Eiseman and the control method of Smith et al has been developed. The code is executed interactively and strongly emphasizes the use of color graphics. User input may be both digital (i.e., from a file or terminal keyboard) and analog (i.e., a graphics cursor or "joydisk"). The 3-D grid system, which is generated by "stacking" a series of 2-D grid systems, may be viewed graphically with provision for enlargement ("zoom") of specific sections of interest.

The grid system may be modified using a variety of techniques which permit redistribution of grid points and redefinition of boundary surfaces. The modification is fully graphics based and provides a variety of grid diagnostics including graphical representation of the Jacobian, angle of intersection of grid lines and distribution of grid points versus distance along any specified coordinate line.

The various features of the code may be "command-driven" by the user. Consequently, the user may proceed to develop, diagnose and modify the grid system as desired.

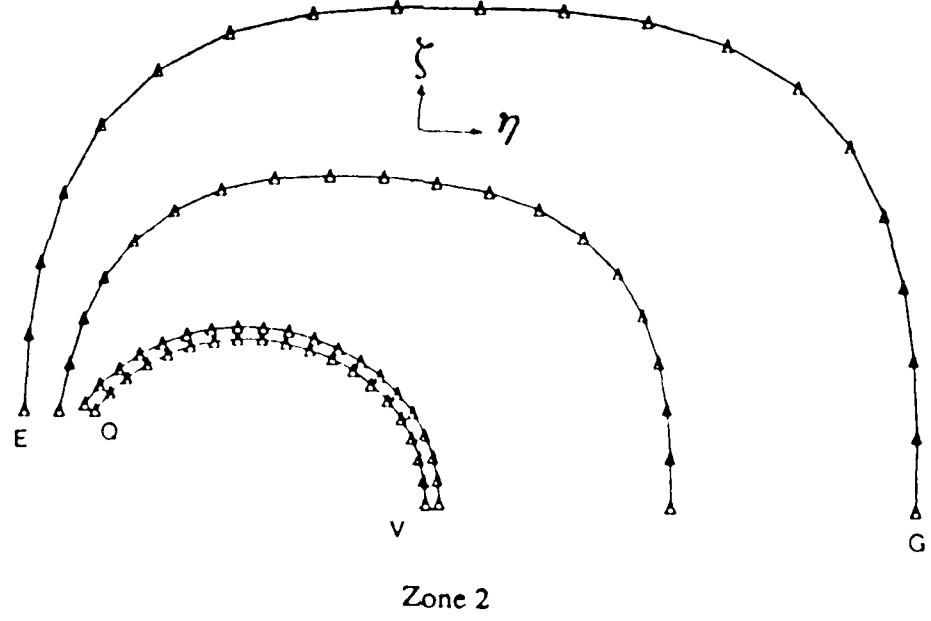
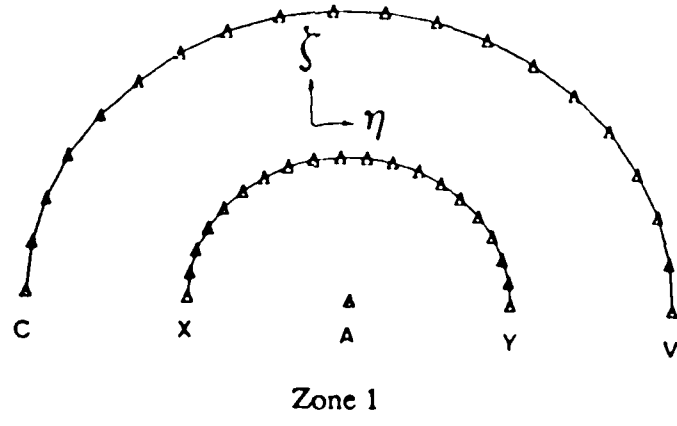
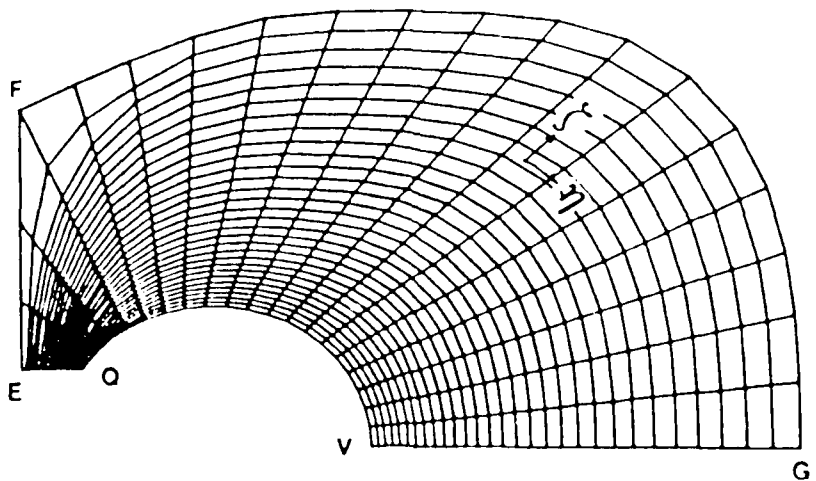
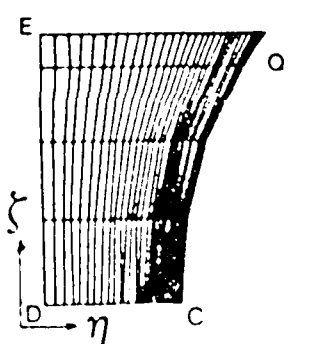


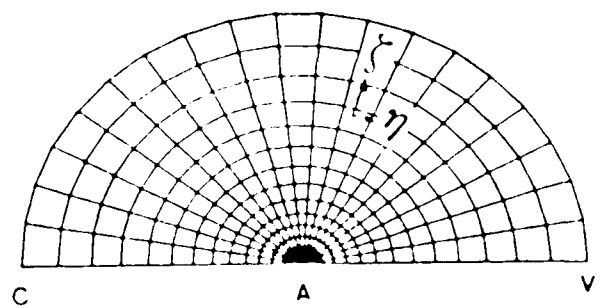
Figure 2-10: Intermediate Surfaces for Zones 1 and 2



Zone 2



Zone 3



Zone 1

Figure 2-11: Subgrids at Section Upstream of Nozzle Exit

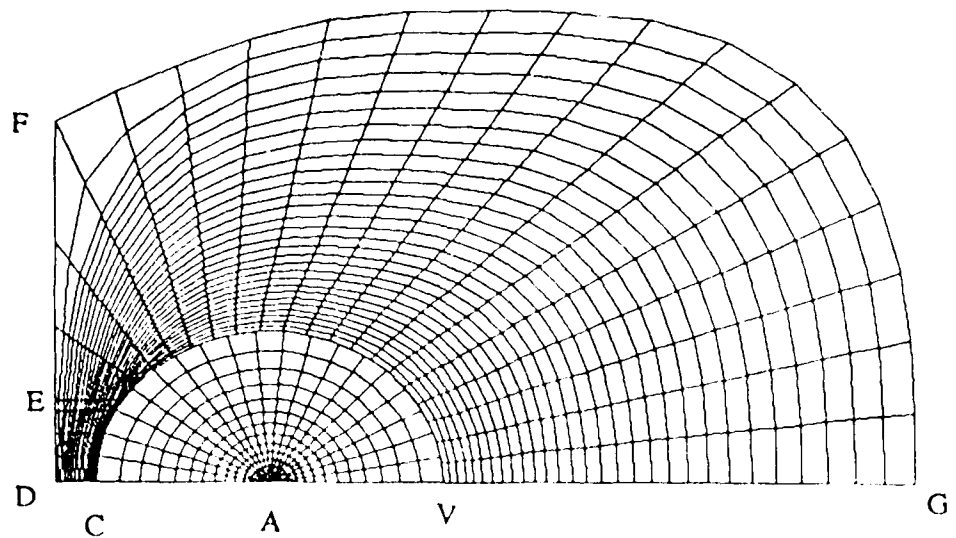


Figure 2-12: Composite Grid at Section Upstream of Nozzle Exit

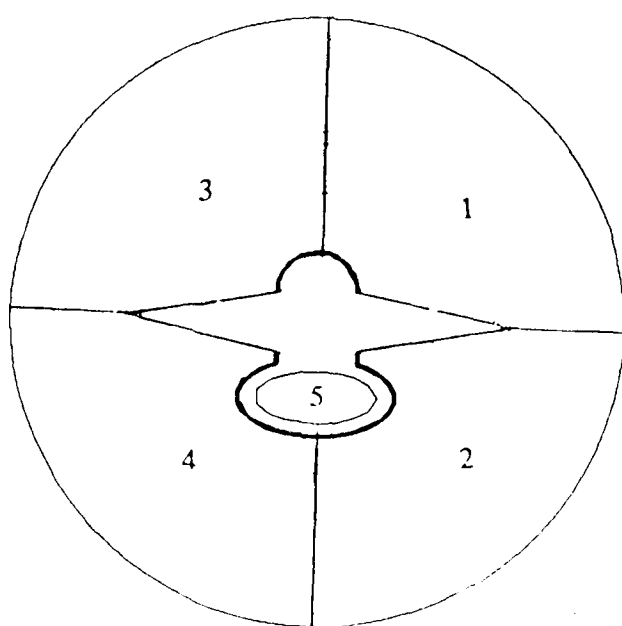
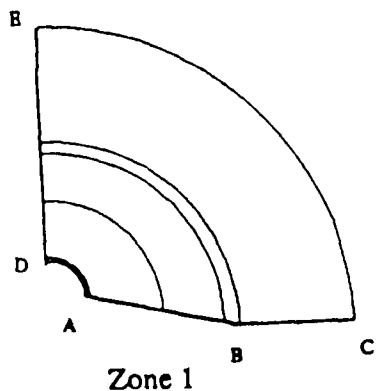
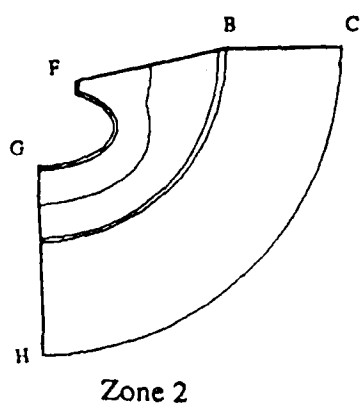


Figure 2-13: Schematic of Aircraft Section Grid



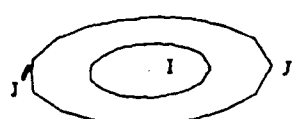
Inner boundary: Circular (AD).
 Outer boundary: Circular(EC).
 Intermediate surfaces (4):
 Points: 20 in circumferential direction.
 30 in radial direction.

Zone 3: Reflection of Zone 1 about DE.



Inner boundary: Inlet exterior (FG).
 Outer boundary: Circular (CH).
 Intermediate surfaces (4):
 Points: 20 in circumferential direction.
 30 in radial direction.

Zone 4: Reflection of Zone 2 about GH.



Zone 5

Inner boundary: Singularity corresponding
 to center of inlet (I).
 Outer boundary: Elliptic (JJ'J).
 Intermediate Surfaces (1): Elliptic
 Points: 17 in circumferential direction.
 10 in radial direction.

Figure 2-14: Intermediate Surface Structure for Aircraft Section

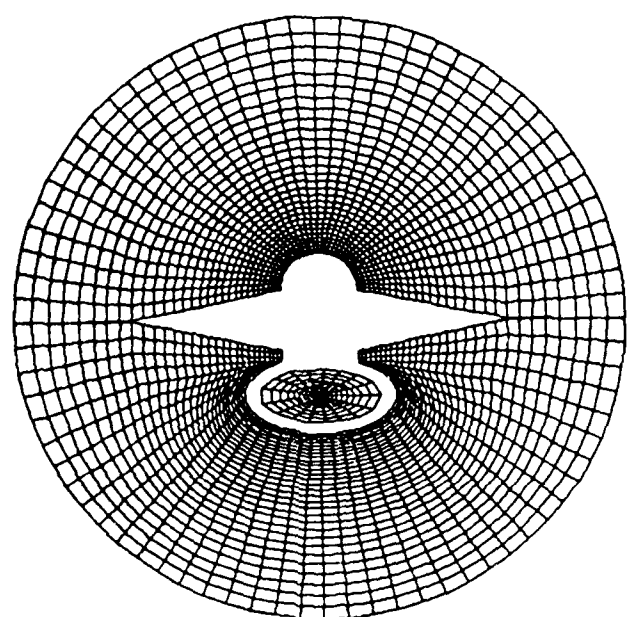


Figure 2-15: Final Grid for Aircraft Section

3. Simulation of Nozzle Flows

3.1. Introduction

The principal objectives of this research are to develop and evaluate the ability to simulate complex nozzle flows. One of the fundamental characteristics of such flows is the existence of two generally parallel streams of flows - internal and external - which meet downstream of some trailing edge to form a mixing layer, the properties of which are of some significance. Of the two generic types of nozzle configurations - axisymmetric and non-axisymmetric - the latter category is chosen as the focus of this research. This choice is governed by the existence of experimental data base for verification purposes. We emphasize that the complexity of the resultant flow structure for both axisymmetric and non-axisymmetric nozzles is expected to be similar.

In subsection 3.2, a brief description of the experiments of Mason and Abeyounnis [46] is provided. Fig. 3-1 is a picture of the configuration under consideration. Since the experiments employed for validation display vertical and horizontal symmetry (zero angle of attack and yaw), this assumption is integral to the computations. The flow is computed in one quadrant of the nozzle only (region ABCDEFGH in Fig. 3-1). A topological discussion follows in subsection 3.3 which describes the physical to computational plane mapping. The full Reynolds averaged Navier-Stokes equations in mass averaged variables and two different turbulent eddy viscosity models for different regions of the flow constitute the theoretical model and are described in subsection 3.4. The discretization and numerical solution of the governing equations is outlined in subsection 3.5. Some details of the implementation of the eddy viscosity models in the flow field are provided in subsection 3.6. Subsection 3.7 describes the coordinate transformation employed (grid structure) and certain geometrical simplifications made so that the problem is more amenable to solution. A brief description of the boundary conditions employed follows in subsection 3.8. Numerical details such as the CPU time required and history of computation are discussed in subsection 3.9. In subsection 3.10, the numerical results are compared with experimental measurements. These comparisons are based on static pressure

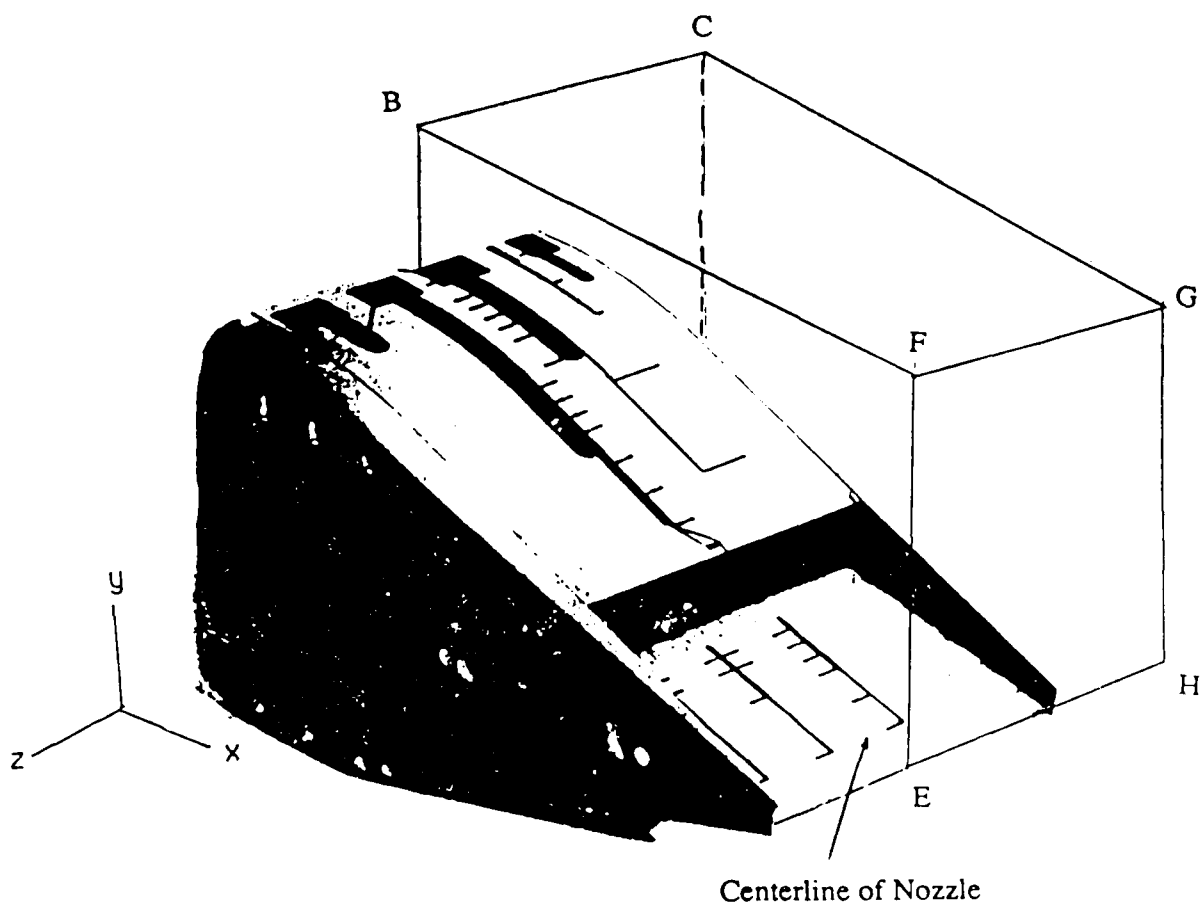


Figure 3-1: Non-Axisymmetric Nozzle in Low-Expansion Configuration. From [46]

measurements. A preliminary analysis of the flow field is discussed in subsection 3.11.

3.2. Brief Description of Experiments

The experiments employed for comparison determine the geometry and flow conditions under consideration. These experiments were performed by Mason and Abeyounis [46] in the Langley 16-Foot Transonic Tunnel (Fig. 3-2)- a single-return, continuous-flow, atmospheric wind tunnel with an octagonal test section. The experiments are performed at wind-off conditions for a range of freestream Mach numbers from 0.6 to 1.2 on two non-axisymmetric wedge nozzles. For each Mach number, two expansion ratios, high (1.20) and low (1.06), are documented. The focus of this research concerns the only supersonic case documented (Mach number = 1.2) in the low expansion configuration described. The high-expansion-ratio configuration was not investigated. The flow conditions are provided in Table 3-1. The nozzle consists of five components: two sidewalls, an upper and a lower flap and a wedge centerbody. Side and top views of the internal and external geometry of the nozzle configuration are provided in Fig. 3-3. This figure also provides the precise dimensions employed in the numerical simulation. Certain geometrical modifications, which are also marked, (subsection 3.7) are made so that the problem is more amenable to solution. The nozzle configuration is instrumented with 14 rows of static-pressure orifices, the locations of which are described in subsection 3.10. Further details of the model instrumentation and techniques used may be found in [46] and will be omitted here for the purposes of brevity.

3.3. Topological Discussion

This subsection establishes certain conventions and definitions which help in the description of the implementation of the theoretical model and numerical algorithm. For the purposes of the subsequent discussion, the general regions of the flow field are shown in Fig. 3-4 which displays the top and side views (the streamwise direction is from left to right in both) of the nozzle. Five boundary layers may be defined. Boundary layers 1 through 3 constitute parts of the internal flow and exist on the flap inner wall, inner sidewall and on

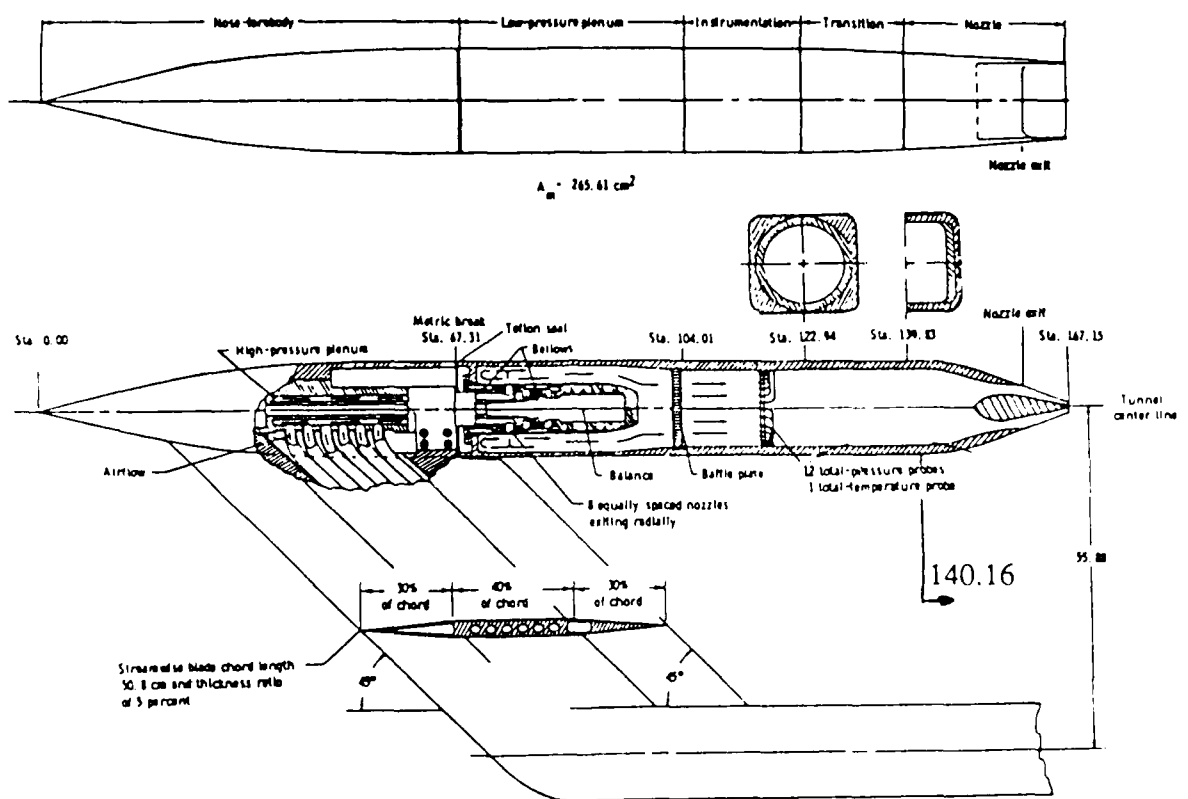


Figure 3-2: Air-Powered Nacelle Model with Nonaxisymmetric Plug Nozzle Installed. From [46]

Table 3-1: Flow Conditions in Experiment

External Flow:

M_{∞}	$T_{t,t}(K)$	$P_t(kPa)$	$N_{Re} (/m)$
1.20	339.03	101.04	12.92×10^6

$$T_w = 331.4 \text{ K} = \text{Adiabatic Wall Temperature}$$

Internal Flow:

$NPR = 2.0$	Upstream Mach No. = 0.19
$T_{t,j} = 300.2 \text{ K}$	$P_{t,j} = 83.3 \text{ kPa}$

Legend:

M_{∞} - Freestream Mach number

$T_{t,t}$ - Average tunnel total temperature

P_t - Average tunnel total pressure

$T_{t,j}$ - Average jet total temperature

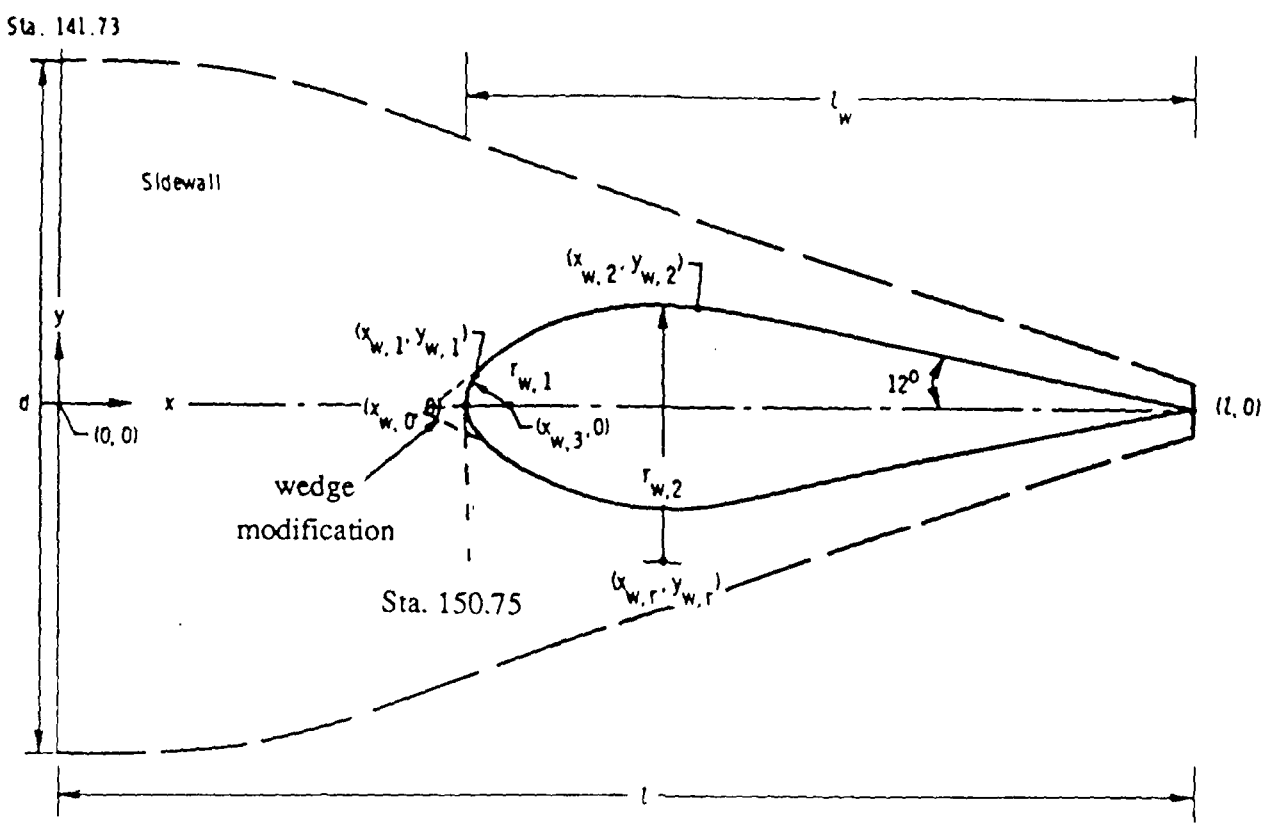
N_{Re} - Reynolds number

T_w - Wall Temperature

NPR - Nozzle Pressure Ratio ($P_{t,j}/P_{\infty}$)

the wedge respectively. Boundary layers identified 4 and 5 occur in the external flow on the flap outer wall and the outer sidewall respectively. The mixing layer is formed when the internal and external flows meet at the trailing edge of the flap. Under the assumptions of subsection 3.7, there is no mixing layer downstream of the sidewall.

The employment of body-fitted grids and general coordinates permits the entire nozzle (including internal, external and mixing layer flows) to be mapped onto a unit cube. This is depicted schematically in Fig. 3-5. The ξ (index i) direction corresponds to the generally streamwise (x) direction, the η coordinate increases in the generally spanwise (z) direction and the ζ coordinate is arranged so that the coordinate system ξ - η - ζ is right-handed with y increasing in the general ζ direction. The index k corresponding to the interior flap surface is denoted k_{nozzle} , while that for the shell is denoted k_{shell} . Similarly, the index j corresponding to the interior sidewall surface is denoted j_{nozzle} and j_{shell} is employed for



Geometrical Modifications:

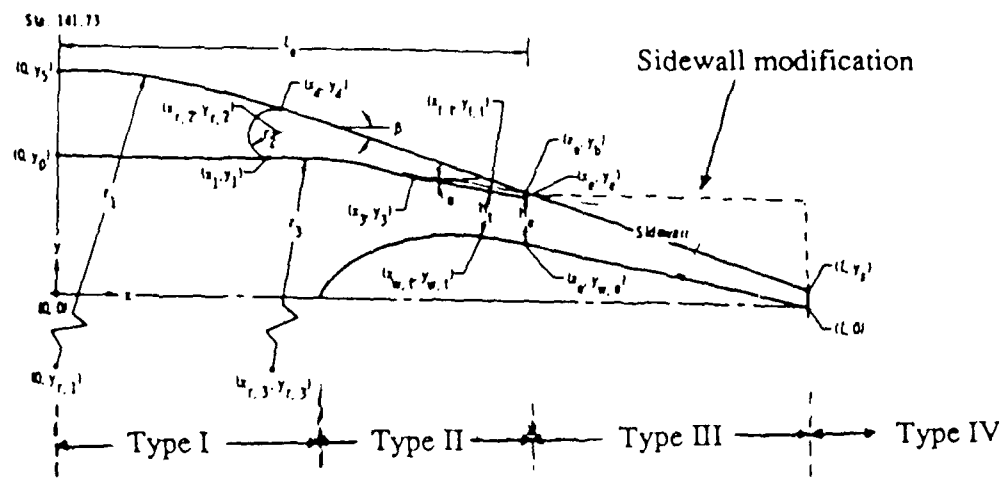
$$x_{w,0} = 8.620$$

d	15.748
l	25.417
l_w	16.398
$r_{w,1}$. . .	0.958
$r_{w,2}$. . .	5.955
$x_{w,0}$. . .	9.019
$x_{w,1}$. . .	9.303
$x_{w,2}$. . .	14.729
$x_{w,3}$. . .	9.477
$x_{w,r}$. . .	13.491
$y_{w,1}$. . .	0.681
$y_{w,2}$. . .	2.272
$y_{w,r}$. . .	-3.553

9.977 (private comm. W. Abeyounis)

(a) Wedge geometry.

Figure 3-3: Internal and External Geometry. From [46]



	Low expansion ratio		Low expansion ratio		Low expansion ratio
A_0/A_1	1.000	$y_{w,1}$	14.366	$y_{w,0}$	2.048
n_0	1.707	y_1	2.274	$y_{w,1}'$	2.359
n_1	1.611	y_2	11.973	y_0	4.939
t	25.427	y_3	7.553	y_1'	4.939
t_0	15.782	y_4	3.856	y_2	4.321
x_1	23.622	y_5	3.755	y_3	6.634
r_2	0.071	$y_{l,1}$	5.931	y_4	7.074
r_3	18.220	$y_{l,1}'$	-15.748	y_5	8.443
r_4	15.782	$y_{l,2}$	5.809	θ, \deg	13.647
$r_{l,1}$	14.603	$y_{l,2}'$	-13.282	Δ, \deg	0.000
$r_{l,2}$	7.274	$y_{l,3}$	0.606		
$r_{l,3}$	7.274	y_5'			

Geometrical Modifications:

$$y = 3.775$$

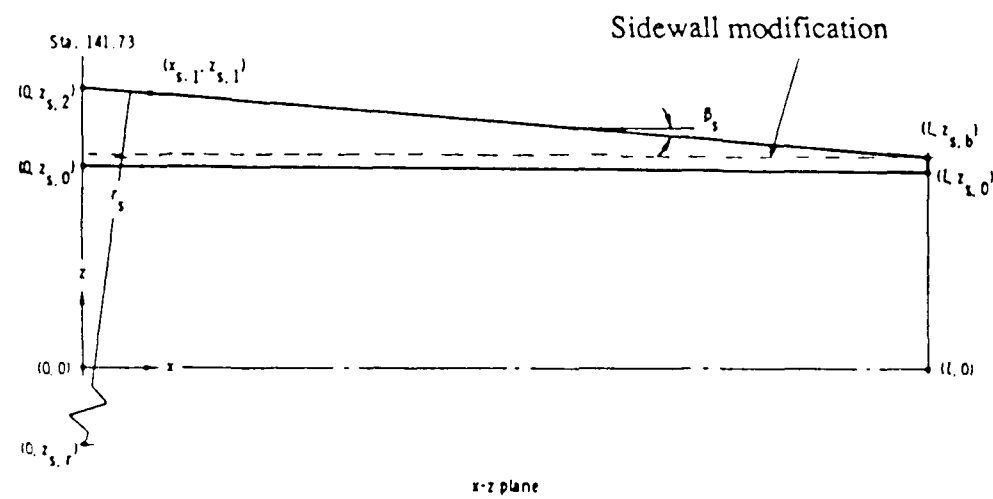
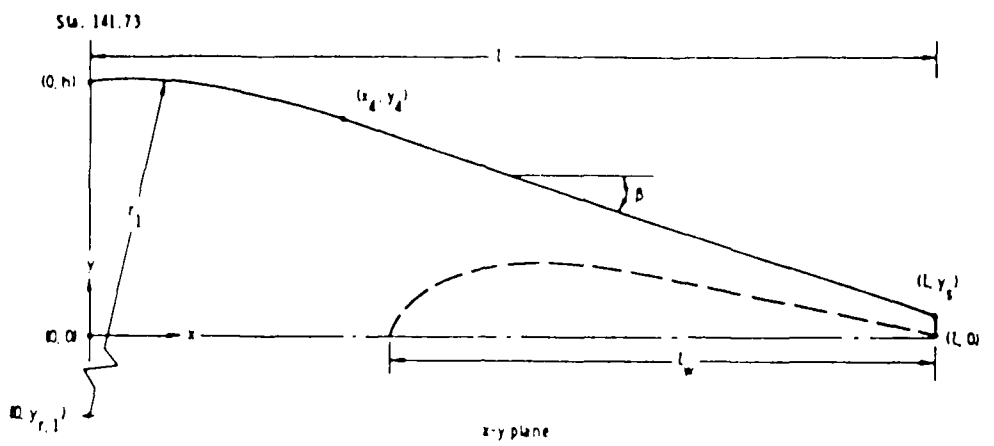
$$b$$

$$y = 3.775$$

$$s$$

(b) Flap geometry.

Figure 3-3 (contd.): Internal and External Geometry. From [46]



Geometrical Modifications:

$z_s = 6.307$
s,b

$z_s = 6.307$
s,2

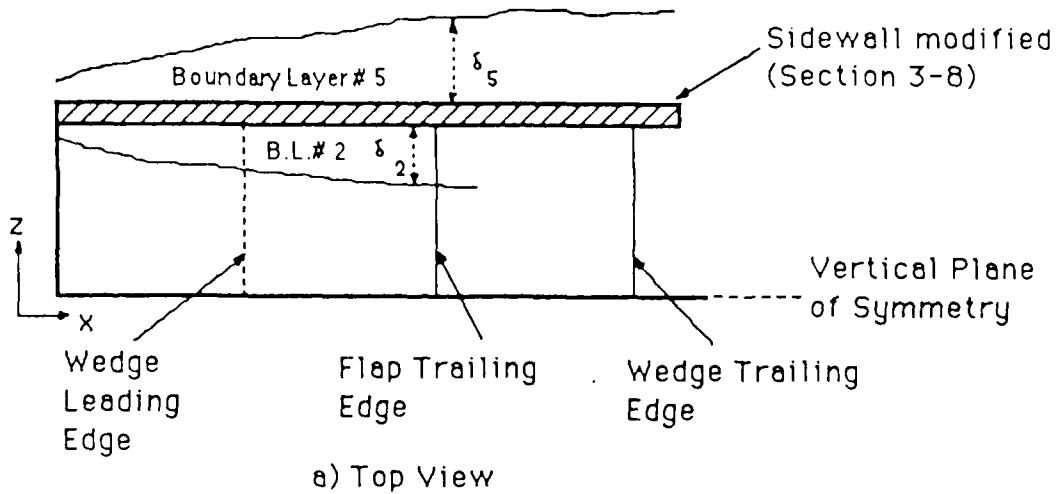
$\beta_s = 19.16^\circ$

$\beta_s = 0^\circ$

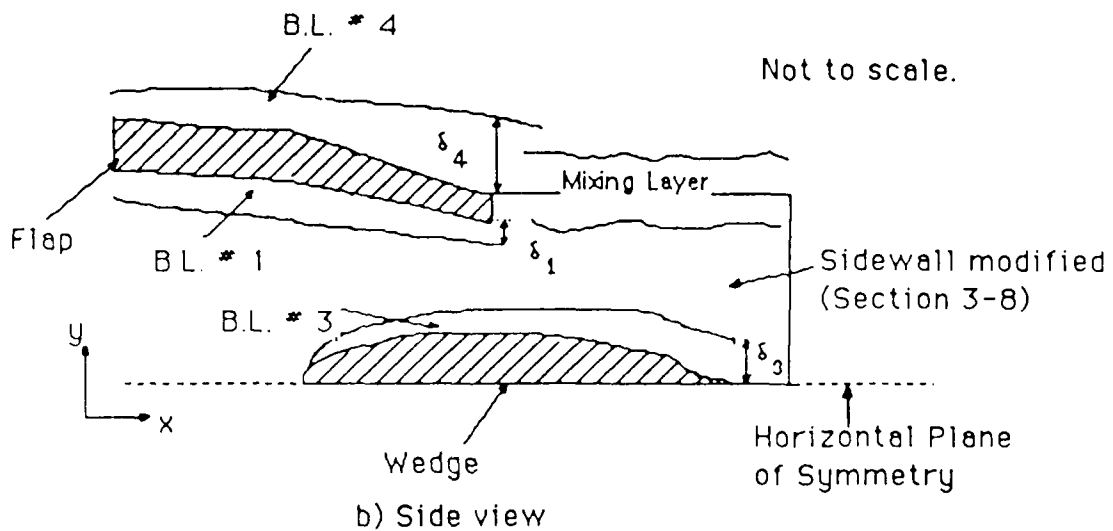
$h \dots$	7.374
$l \dots$	25.417
$l_w \dots$	16.398
$r_1 \dots$	23.622
$r_s \dots$	23.622
$x_4 \dots$	7.553
$z_{s,1} \dots$	1.957
$y_4 \dots$	6.634
$y_{r,1} \dots$	23.622
$y_s \dots$	0.606
$z_{s,0} \dots$	6.287
$z_{s,1} \dots$	8.555
$z_{s,2} \dots$	8.636
$z_{s,b} \dots$	6.604
$z_{s,r} \dots$	23.622
$\Delta \text{deg.} \dots$	18.64
$\beta_s \text{ deg.} \dots$	4.753

(c) Sidewall geometry.

Figure 3-3 (contd.): Internal and External Geometry. From [46]

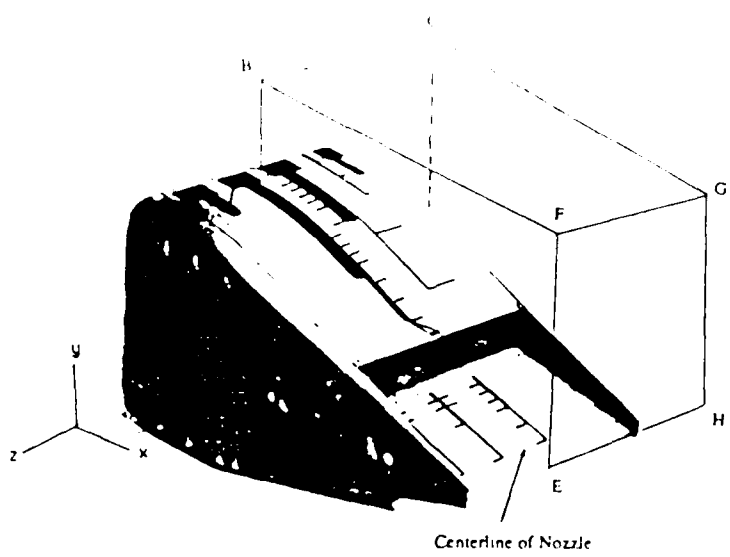


a) Top View

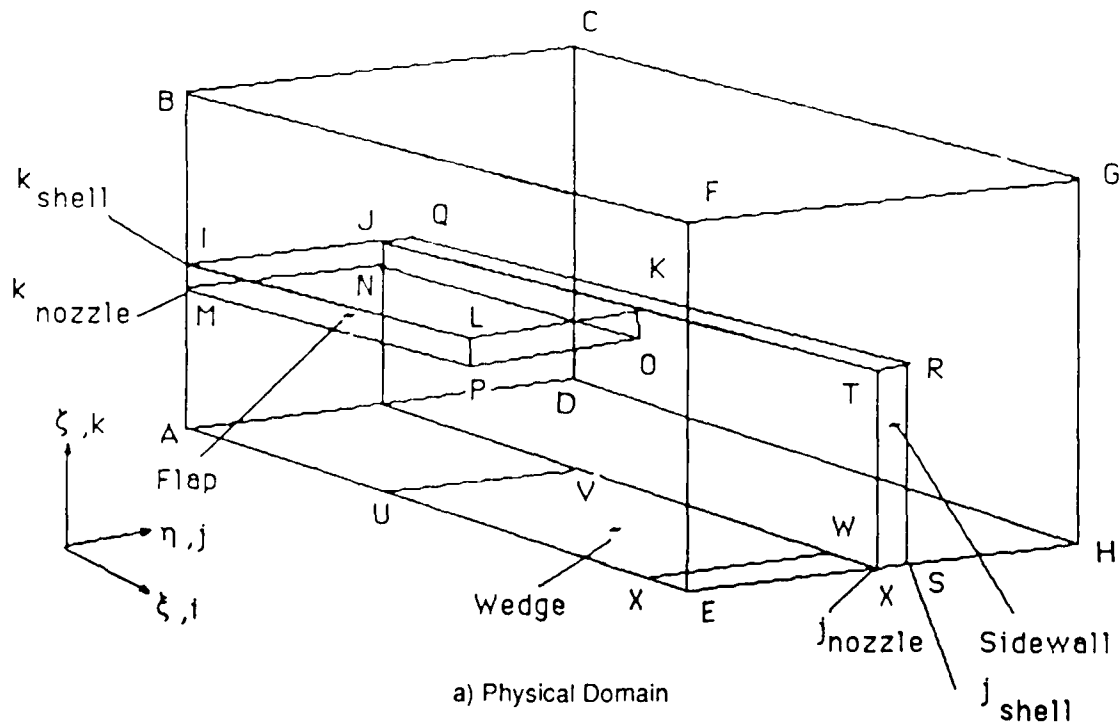


b) Side view

Figure 3-4: General Flow Structure - Top and Side Views



b) Computational Domain



a) Physical Domain

Figure 3-5: Physical and Transformed Domains - Nonaxisymmetric Nozzle

the exterior sidewall surface. By construction (subsection 3.7),

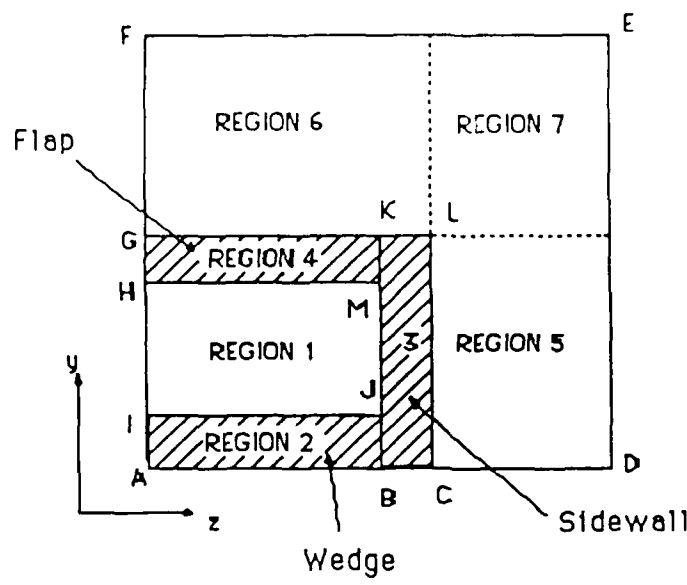
$$\begin{aligned} j_{shell} &= j_{nozzle} + 1 \\ k_{shell} &= k_{nozzle} + 1 \end{aligned} \quad (6)$$

In Fig. 3-5 the upstream boundary is ABCD, a part of which (height AM, width MN) corresponds to internal flow. The downstream boundary is EFGH and is located some distance downstream of the wedge trailing edge. Details of dimensions are provided in a later subsection. The plane of horizontal symmetry is denoted ADHE, a part of which (UVWX) corresponds to the upper surface of the wedge. ABFE is the vertical plane of symmetry. The freestream boundaries (BFGC and CDHG) are located far enough away from the nozzle for the application of freestream boundary conditions. The flap outer and inner surfaces are mapped on the planes IJKL and MNOP respectively. For purposes of clarity, only two adjacent boundaries (QR and RS) of the external sidewall are shown in the figure. The sidewall extends beyond the flap trailing edge up to the wedge trailing edge as is clear from the figure of the nozzle (Fig. 3-3). Some assumptions on the flap trailing edge and the sidewall are described later.

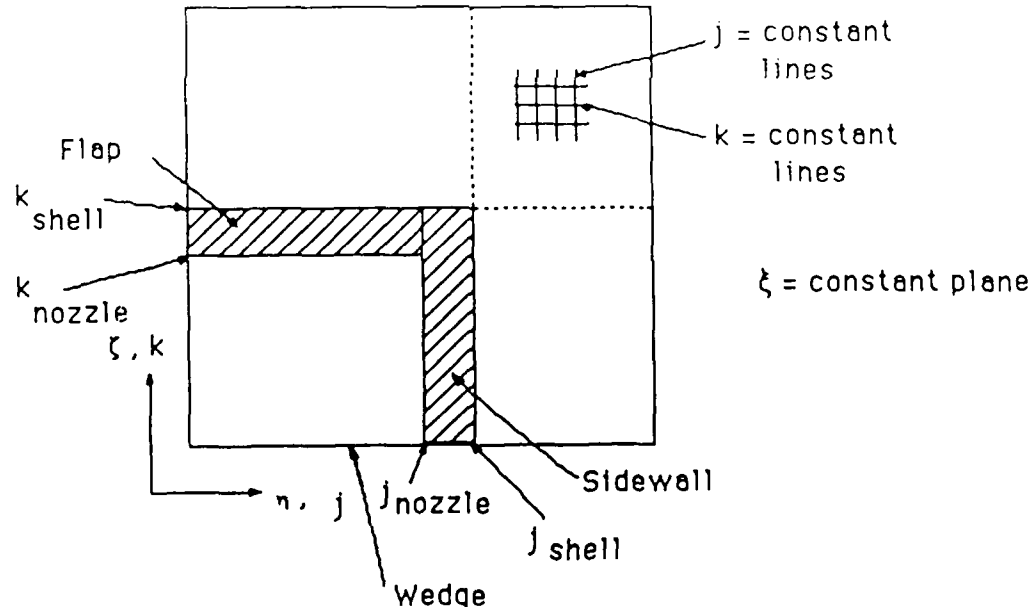
The body-fitted grid is generated in axis-normal ($\xi = \text{constant}$) planes for simplicity. A general physical plane and the corresponding computational plane is shown in Fig. 3-6. At any cross section, the following naming convention is employed.

- Region 1 : internal flow ($1 \leq k \leq k_{nozzle}$ and $1 \leq j \leq j_{nozzle}$)
- Region 2 : wedge (if it exists at the streamwise location) (" $k < 1$ ")
- Region 3 : sidewall (if it exists at the streamwise location) ($k < k_{shell}$ and " $j_{nozzle} < j < j_{shell}$ ")
- Region 4 : Flap (if it exists at the streamwise location) ($j < j_{nozzle}$ and " $k_{nozzle} < k < k_{shell}$ ")
- Regions 5, 6 and 7 : external flow ($k > k_{shell}$ or $j > j_{shell}$)

The indices in quotes indicate areas where no grid lines exist. Four distinct types of $\xi=\text{constant}$ planes may be identified. This distinction is based on the streamwise distance which determines the existence of the flap, wedge or sidewall at each section. The range



a) Physical Region



b) Computational Region

Figure 3-6: General Physical and Corresponding Transformed Plane

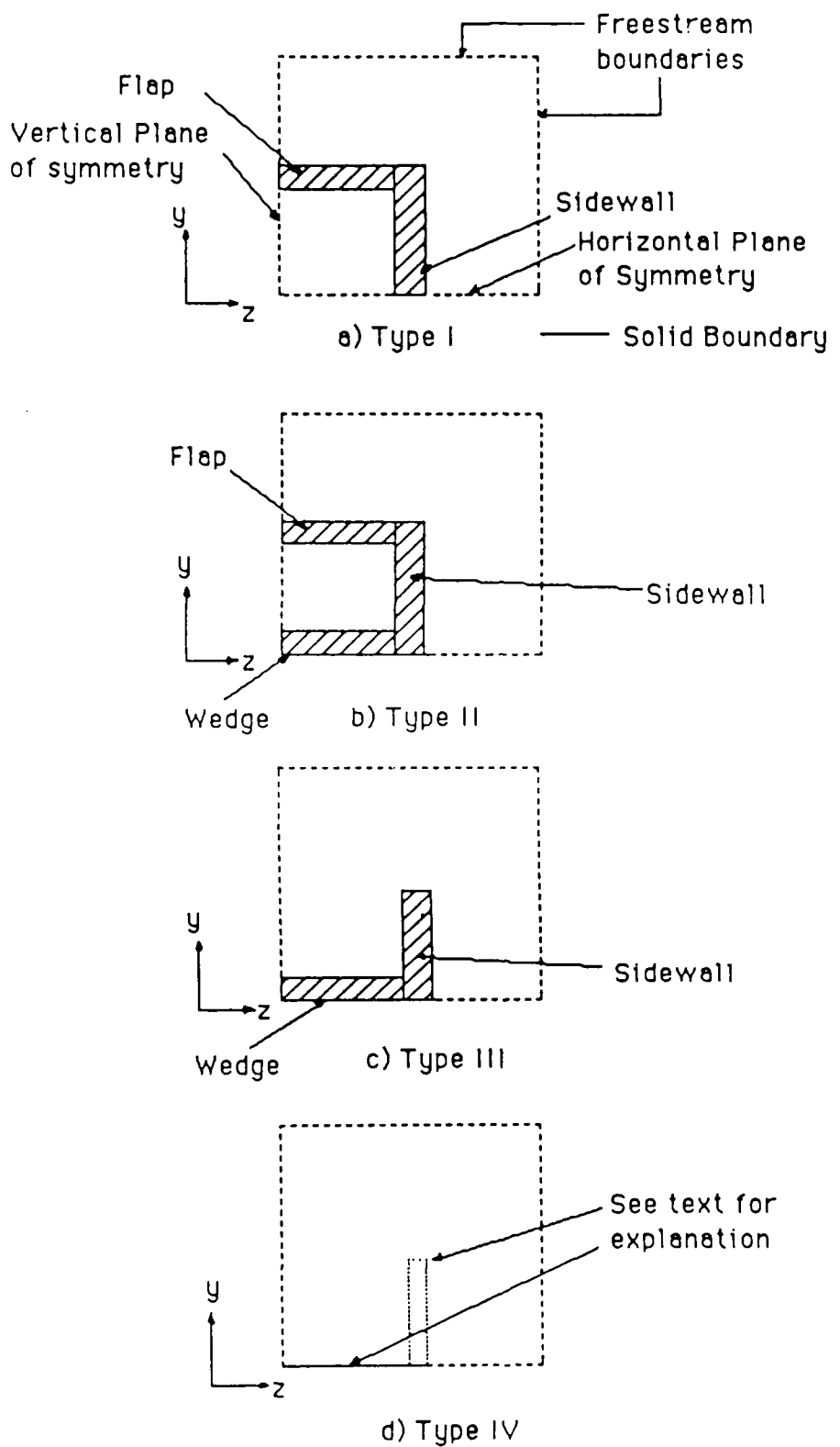


Figure 3-7: Different Types of Cross Sections

of x values for each type of cross section is shown in Fig. 3-3 (b).

- Type I cross-section: This type of cross-section occurs between the upstream boundary and the leading edge of the wedge (see Fig. 3-7 (a)). Note that the flap trailing edge is downstream of the wedge leading edge. In the physical plane of Fig. 3-6 (a), the line IJ merges with AB (region 2 vanishes). The line GK represents the outer surface of the flap and HM represents the inner surface of the flap. The lines CL and BK represent the outer and inner sidewall faces respectively. The boundary FED is the freestream boundary.
- Type II cross section: This type of cross section occurs between the leading edge of the flap and the trailing edge of the flap (see Fig. 3-7 (b)). The major difference between this type of cross section and that of Type I cross section is that region I is finite and corresponds to the wedge cross section.
- Type III cross section: Beyond the flap trailing edge but before the wedge trailing edge, the region (GKHM in Fig. 3-6) is no longer solid (Fig. 3-7(c)). The region KLCB continues to represent the sidewall.
- Type IV cross section: At a section downstream of the wedge trailing edge (which occurs at the same streamwise location as the sidewall trailing edge in the experiment), there are no solid boundaries in the $\xi = \text{constant}$ planes. The computations extend some distance (a few wedge boundary layer thicknesses) beyond the wedge trailing edge (subsection 3.7) to prevent corruption of data in the region of interest due to the downstream boundary conditions outlined in subsection 3.8. Since there is no experimental data available downstream in the wake region, in the computation we assumed for simplicity that a flat plate abuts the wedge trailing edge and that the sidewall extends to the computational downstream boundary. Under this assumption, a Type IV cross section is topologically similar to a Type III section and hence, the sidewall is shown dashed in Fig. 3-7 (d) indicating that it exists only in the computation.

3.4. Theoretical Model

A detailed description of the theoretical model and numerical algorithm may be found in [47] and is omitted here for the purposes of brevity. The governing equations are the 3-D full mean compressible Navier-Stokes equations using mass averaged variables [48]. Written in strong conservation form [49] and employing the transformed variables $\xi(x,y,z)$, $\eta(x,y,z)$ and $\zeta(x,y,z)$, the equations are

$$\frac{\partial U}{\partial t} + \frac{\partial F}{\partial \xi} + \frac{\partial G}{\partial \eta} + \frac{\partial H}{\partial \zeta} = 0 \quad (7)$$

where,

$$U = \frac{1}{J} \begin{Bmatrix} \rho \\ \rho u \\ \rho v \\ \rho w \\ \rho e \end{Bmatrix} \quad (8)$$

$$J = \frac{\partial(\xi, \eta, \zeta)}{\partial(x, y, z)} \quad (9)$$

(u, v, w) are the Cartesian velocity components in the (x, y, z) coordinates. The density ρ , static pressure p and static temperature T are related through the equation of state $p = \rho RT$ where R is the gas constant and J is the Jacobian of the transformation. The total energy per unit mass is given by $e = e_i + 0.5(u^2 + v^2 + w^2)$, where the internal energy per unit mass e_i is equal to $C_v T$ and C_v is the specific heat at constant volume. The flux vectors F , G , and H include the effects of turbulence in the eddy viscosity (ϵ) formulation. The molecular dynamic viscosity μ is given by Sutherland's law. The molecular and turbulent Prandtl numbers, Pr and Pr_t , are 0.73 (air) and 0.9 respectively.

In the vicinity of a surface, a special subset of the Navier-Stokes equations is employed [47]. Two types of sublayer regions are defined: (1) "line sublayer" and (2) "corner sublayer". These two different regions are distinguished by their relative size in respect to the principal radii of curvature of the surface. The line sublayer corresponds to a sublayer whose height (i.e., approximately the height of the transition wall region of the turbulent boundary layer) is small compared to the principal radii of curvature of the surface. For this category, the local surface appears "flat" within the scale of the sublayer (i.e., surface curvature effects may be neglected). The "corner sublayer" corresponds to a

sublayer where the height of the sublayer is comparable or larger than one of the local principal radii of curvature of the surface. A sharp corner (i.e., the local intersection of two planes) is a corner sublayer since one principal radius of curvature is zero. The code requires that the corners be 90 degrees, a condition satisfied by the nozzle under consideration.

For a line sublayer, the assumption is that the effects of diffusion of momentum and energy in the direction normal to the surface are substantially greater than those in the plane. The governing equations reduce to a set of three ordinary differential equations [44, 47] which are solved with the Keller Box Scheme [50].

In the vicinity of a corner, the corner sublayer equations [44, 47] are solved. These equations are also obtained asymptotically from the mean compressible Navier-Stokes equations and reduce to two coupled nonlinear partial differential equations. The solution of these equations is obtained with second-order accurate finite differences and solved using Newton's method.

The two-layer turbulent eddy viscosity model of Baldwin and Lomax [51] is employed in regions where no mixing layer exists. In this model, the inner eddy viscosity is given by

$$\epsilon_i = \rho(\kappa/l)^2\omega \quad (10)$$

where $\kappa = 0.40$ is von Karman's constant, l is the Buleev length scale [52, 53, 54], D is the Van Driest damping factor and ω is the absolute value of the vorticity ($\omega=|\nabla \times \vec{v}|$)

The outer eddy viscosity is given by

$$\epsilon_o = \rho k C_{cp} F_{wake} F_{Kleb} \quad (11)$$

where k (= 0.0168) and C_{cp} (see below) are constants. The outer function F_{wake} is given by

$$F_{wake} = l_{max} F_{max} \quad (12)$$

and,

$$F_{max} = \max(F_{outer}), \quad F_{outer} = l \omega D \quad (13)$$

and the maximum is evaluated over the entire boundary layer. The quantity l_{max} is the

value of l where the maximum value of F_{outer} occurs. The value of Klebanoff intermittency correction in Eqn. 11 is given by

$$F_{\text{Kleb}} = \left(1 + 5.5 \frac{C_{\text{Kleb}} l}{l_{\max}}\right)^{-1} \quad (14)$$

where C_{Kleb} is a constant.

Recent calculations [55] have established that the constants C_{cp} and C_{Kleb} are functions of the Mach number and the wake parameters. For the freestream conditions established in Table 3-1, the values of these two constants were determined to be 1.3 and 0.3, respectively.

The inner and outer eddy viscosity models are combined to form the turbulent eddy viscosity ϵ in the following manner. First, profiles of ϵ_i and ϵ_o are obtained on each coordinate line emanating from the boundary. This implies that the coordinate lines are approximately orthogonal within the boundary layer. The first point nearest the boundary at which ϵ_i exceeds ϵ_o is denoted the "cross-over point". The turbulent eddy viscosity ϵ is then equal to ϵ_i for all points between the boundary and the cross-over point, and is equal to ϵ_o for all points above and including the cross-over point. Further details of the implementation of the Baldwin Lomax eddy viscosity model in the vicinity of corners (internal and external) are outlined in subsection 3.6.

For the free shear layer region (see Fig. 3-4), the mixing layer model [11, 56] is employed. In this case,

$$\epsilon = \rho l^2 |\bar{\omega}| \quad (15)$$

where,

$$l = C_{\text{mix}} U / |\bar{\omega}|_{\max} \quad (16)$$

and

$$U = |\bar{v}|_{\max} - |\bar{v}|_{\min}, \quad C_{\text{mix}} = 0.13 \quad (17)$$

The search for $|\bar{\omega}|_{\max}$ is conducted in a region on either side of the location of $|\bar{v}|_{\min}$ (subsection 3.6).

It may be noted that this set of governing equations in conjunction with the numerical algorithm employed (see subsection 3.5) is extendable to unsteady flows under the assumption that the characteristic turbulent diffusion time across the computational sublayer i.e.,

$$t_{diff} = \frac{z_m^2 \rho_r}{(\mu_r + \epsilon_r)} \quad (18)$$

is small compared to the characteristic time scale of the unsteady mean motion t_{mean} . In the above expression, z_m is the height of the computational sublayer, which is typically less than or equal to 60 wall units (i.e., $z_m u_* / v_w < 60$, where u_* is the local friction velocity and v_w is the kinematic viscosity at the wall [21]). The quantities ρ_r , ϵ_r and η_r are characteristic values for the density, molecular dynamic viscosity and turbulent eddy viscosity in the computational sublayer (evaluated, for example, at the edge of the sublayer). By virtue of the use of the unsteady Reynolds-averaged equations, we assumed that the time scale of the unsteady mean motion t_{mean} is similar to the characteristic development time of the mean flow t_c , i.e.,

$$t_{mean} \sim t_c \quad (19)$$

where

$$t_c = \frac{L}{u_\infty}$$

where L is a characteristic length scale of the mean flow (e.g., the airfoil chord in the case of the transonic airfoil computations of Levy [35]), and u_∞ is the characteristic velocity of the mean flow. The use of the computational sublayer technique, therefore, implies

$$t_{diff} \ll t_c \text{ or } t_{diff} \ll t_{mean}$$

Due to the exceedingly small height of the computational sublayer (typically one percent of the boundary layer thickness), this constraint is generally met in practice.

3.5. Numerical Algorithm

The numerical algorithm is a hybrid explicit-implicit technique which combines the explicit finite-difference algorithm of MacCormack [43, 57] for the full mean compressible Navier-Stokes equations and the implicit finite-difference Box Scheme of Keller [50] for the asymptotic form of the mean compressible Navier-Stokes equations in the viscous sublayer and transition wall regions of the turbulent boundary layers.

For the purposes of implementation of the explicit and implicit algorithms, the transformed domain is divided into two types of regions - ordinary and sublayer. These regions are shown in Fig. 3-8 for each type of section. The ordinary region consists of grid points updated by the explicit algorithm while the sublayer regions are resolved with the implicit algorithm. The grid points in the sublayer region are generated separately from the ordinary grid with geometric stretching. The ordinary and sublayer regions are interfaced along the "line of matching points", which is the row of ordinary grid points adjacent to each solid boundary [47].

The explicit algorithm of MacCormack is implemented using a symmetric sequence of time split operators. The method is second-order accurate in both space and time and is relatively easy to program in a numerical code. Further, it is easily and efficiently vectorized and is robust. Its overall stability is relatively insensitive to the initial conditions employed. Thus, the initial condition (typically a guess) need not be particularly close to the final (unknown) solution [44]. A fourth-order pressure damping term [57] is incorporated to prevent numerical instability in the presence of strong shock waves.

The implicit algorithm is employed in the viscous sublayer and transition wall regions of the turbulent boundary layers. This region is denoted the "computational sublayer" or "sublayer" for brevity. This hybrid algorithm has been proven to be very efficient. For a 3-D oblique shock-turbulent boundary layer interaction [47], the hybrid algorithm is a factor of 16 to 21 times faster than a vectorized version of MacCormack's explicit algorithm alone using time-split operators. The matching of the explicit and implicit algorithms is achieved through the stress and heat flux tensors [47] and is omitted here for the purposes of

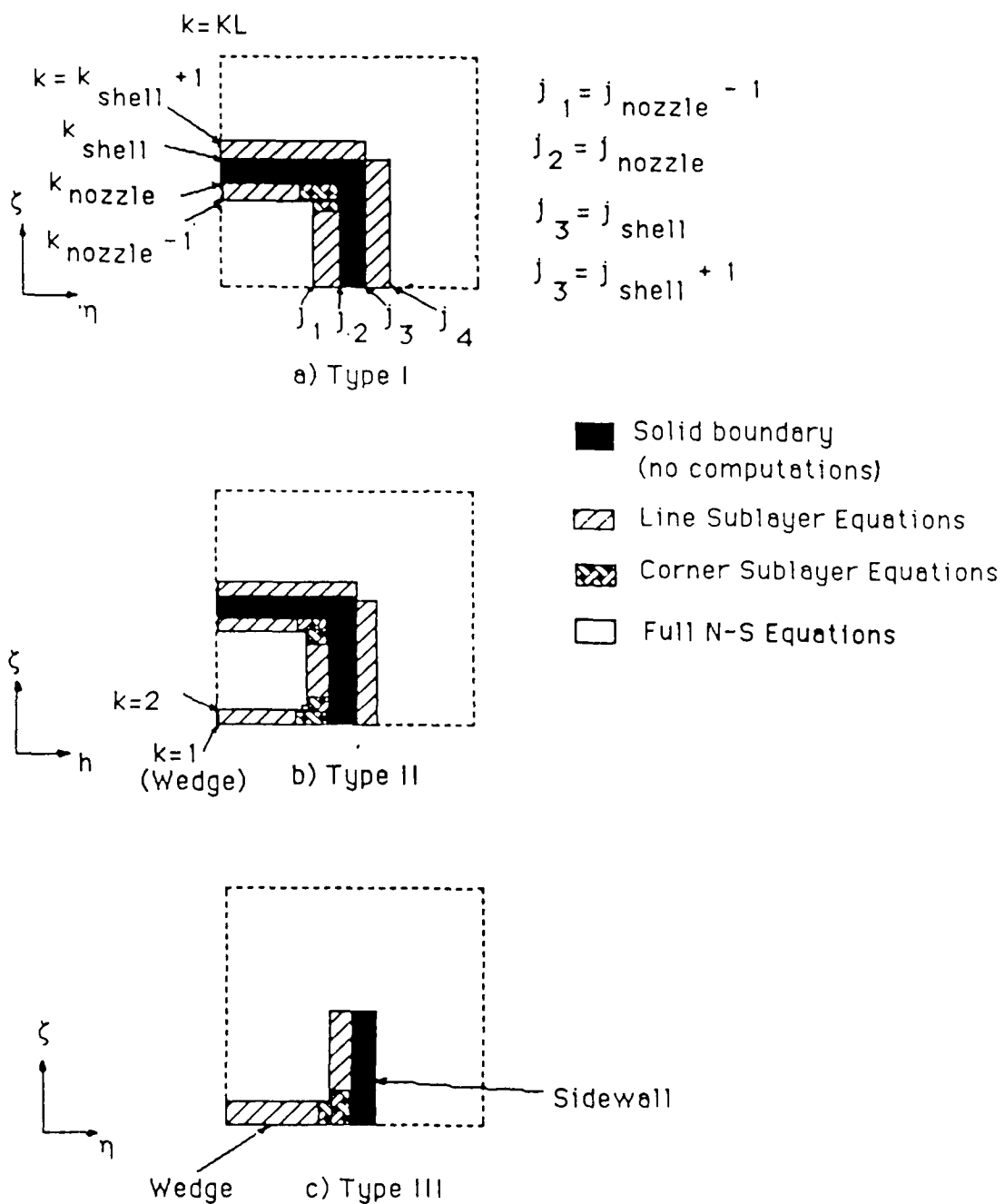


Figure 3-8: Ordinary and Sublayer Regions

brevity.

The governing equations and the Baldwin-Lomax turbulent eddy viscosity model have been successfully applied in conjunction with the hybrid explicit algorithm above for a variety of applications including a 3-D simulated inlet [58], a 3-D sharp fin [59] and a 3-D swept compression corner [60] at supersonic Mach numbers.

3.6. Details of Implementation of Eddy Viscosity

As mentioned in subsection 3.4, the two layer eddy viscosity model of Baldwin Lomax model is employed in regions at close proximity to the wall, and the mixing layer model is employed in the wake region beyond the flap trailing edge. In general, the Buleev length scale is taken to be the distance normal to the surface and ε is defined relative to the local surface boundary layer. In the vicinity of an internal corner, the eddy viscosity (Baldwin Lomax) is implemented by dividing the η - ζ plane into two areas in a manner similar to the method of Hung and MacCormack [61] and detailed in [47]. The approach is illustrated in Fig. 3-9 for the case of the corner formed by the flap and the sidewall in a section of Type II. The line dividing the two areas is taken to be (for example)

$$\zeta = \zeta_{nozzle} - \frac{\Delta\zeta}{\Delta\eta} (\eta - \eta_{nozzle}), \quad (20)$$

where

$$\Delta\zeta = \frac{1}{KL-1}, \quad \Delta\eta = \frac{1}{JL-1}$$

and JL and KL are the total number of points in the η and ζ direction respectively.

For all points in Area I, the inner and outer eddy viscosity profiles are obtained along ζ = constant lines, and the eddy viscosity is switched from the inner to the outer formulation at the location where $\varepsilon_i > \varepsilon_o$. For points in Area II, the inner and outer eddy viscosity profiles are obtained along η = constant lines and a similar procedure is employed. The dividing line formula 20 is chosen for convenience of numerical implementation. The image of eqn 20 in the physical domain is, in general, a curved line. The exact appropriate shape of the dividing line in the physical domain is not known in general and care must be taken to ensure that a pathological shape does not occur.

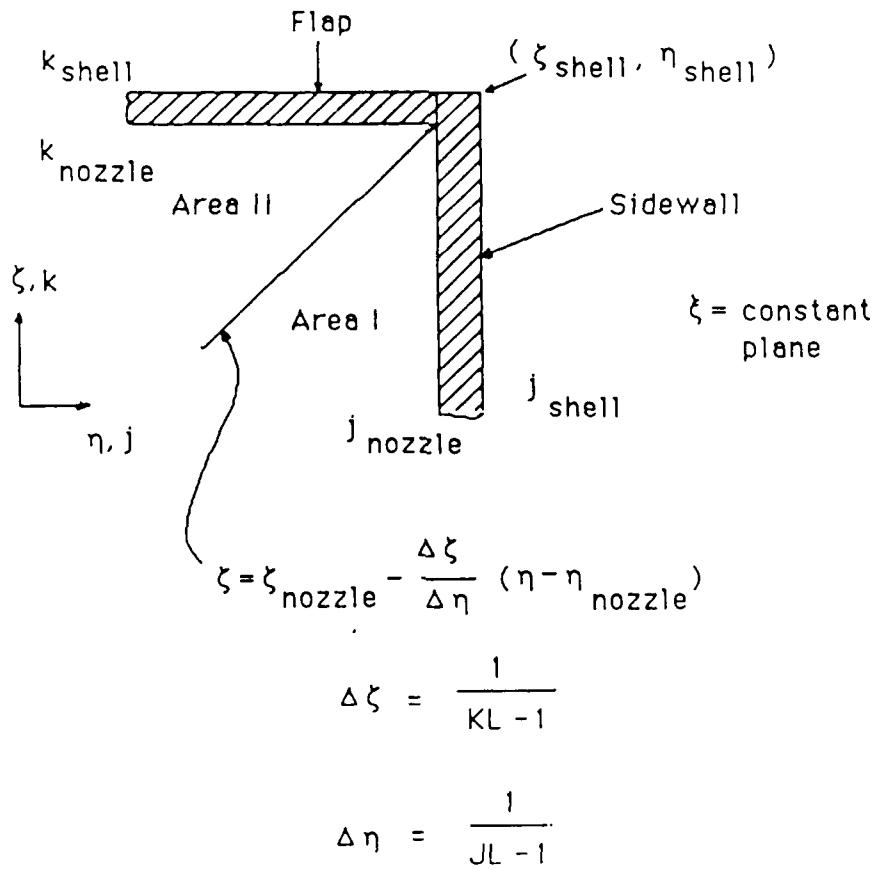


Figure 3-9: Implementation of Eddy Viscosity Model Near Internal Corner

For external corners that occur along the line of intersection of the external flap surface and the external sidewall face (see Region 7 in Fig. 3-6), the implementation of the turbulence model is not clear since the specification of the value of the Buleev length scale is difficult. In this research, a simple engineering approach is taken. The model for the eddy viscosity in Region 7 is obtained by extending on the same eta or zeta line to the line $j=j_{\text{shell}}+k-k_{\text{shell}}$ (see Fig. 3-10). This eliminates the need for defining a Buleev length scale in this region.

In sections of Types I and II, the Baldwin-Lomax model is exclusively employed. In sections of Type III however, both the Baldwin-Lomax and the mixing layer models (subsection 3.4) are applied in different regions of the flow. The areas demarcating the application regions of the two models are shown schematically in Fig. 3-11. In regions a,b and e, the Baldwin-Lomax model is utilized (along $j = \text{constant}$ lines, $k = \text{constant}$ lines ($j < j_{\text{nozzle}}$) and $k = \text{constant}$ lines ($j > j_{\text{shell}}$) respectively. The height h_w (typically about one δ_{wedge}) is a function of the streamwise distance and includes about 10 ordinary grid points. In regions c and d, the mixing layer model is employed. The search for $|\omega|_{\max}$ is conducted from top of region "a" in Fig. 3-11 to the top of the grid (free stream boundary).

3.7. Coordinate Transformation and Geometrical Simplifications

The grid is generated in axis-normal planes and stacked together. A limited number of geometrical simplifications of a non-critical nature are made to simplify the implementation of the numerical algorithm and boundary conditions. For example, a blunt wedge leading edge (as in the experimental configuration), results in a 90° kink in the $\zeta=0$ lines in the internal flow region (see Fig. 3-12) and leads to problems in the computation of ξ derivatives. The wedge is therefore assumed to be sharp by running the tangent at $(x_{w,1}, y_{w,1})$ to the centerline of the nozzle. Other modifications are explained when necessary.

The grid spacing is determined to satisfy the following general constraints [47]:

- Near a solid boundary, the first ordinary grid point away from the boundary must satisfy the condition that $z'_m + < 60$, where z'_m is the height of the sublayer in wall units as defined as in subsection 3.4.

- Near a solid boundary, the first sublayer point away from the boundary must satisfy the condition $z'^* < 3$
- The grid must possess about 15 points inside the boundary layer (including sublayer points) for adequate resolution of gradients.

The grid is stretched in a direction normal to the boundary to satisfy the above constraints without employing a prohibitively large number of points. The maximum stretch factor anywhere in the grid is limited to approximately 1.3. For grid generation purposes, approximate values of the boundary layer thickness (See Table 3-2), friction velocity (u_*) and v_w are determined either with semi-empirical relations or with the 2-D compressible turbulent boundary layer code of York [55]. In Table 3-2, the value of δ_3 is estimated whereas the others are specified. For the computation 8 points are employed in the direction normal to the surface in each sublayer. A brief description of the determination of grid spacing in each of the three principal directions follows.

Table 3-2: Boundary Layer Thicknesses

B.L. #	Notation	Thickness (cm)
1 (Flap inner)	δ or $\delta_{\text{flap inner}}$	0.62 at $x=140.16$ cm
2 (Sidewall inner)	δ_2 or $\delta_{\text{sidewall inner}}$	0.62 at $x=140.16$ cm
3 (Wedge)	δ_3 or δ_{wedge}	0.12 at $x=167.00$ cm
4 (Flap outer)	δ_4 or $\delta_{\text{flap outer}}$	1.69 at $x=140.00$ cm
5 (Sidewall outer)	δ_5 or $\delta_{\text{sidewall outer}}$	1.69 at $x=140.00$ cm

1. X (streamwise) grid spacing: The computational upstream boundary is located at $x=140.16$ cm from the leading edge (see Fig. 3-2). The boundary layer thickness on the sidewall inner surface (δ_2) is utilized to scale the streamwise grid spacing. The axial planes are arranged to provide at least five planes inside the pressure rise (internal flow) with increased concentration of planes in the shock-boundary-layer interaction region immediately downstream of the flap trailing edge. The last station is placed about four δ_2 downstream of the wedge trailing edge. Depending upon the total number of planes

employed, two cases are identified: Case I with 32 planes and Case II (proposed) with 64 planes. In this report only Case I is discussed. The x-locations of each plane are shown in Fig. 3-13 and values are provided in Table 3-3.

2. Y (vertical) grid spacing: The y direction extends normal to the horizontal plane of symmetry. Fig. 3-14 shows typical grids at three sections of Types I, II and III respectively. The total number of points in this direction (for both cases) is 50 (= KL), with 30 points inside the nozzle ($k_{nozzle} = 30$) and 20 points outside the nozzle. To avoid compression of ζ grid lines originating inside the nozzle, the sidewalls are modified to be straight (horizontal) from the trailing edge of the flap. This corresponds to changing the value of y_s from 0.606 cm to 3.775 cm. Since the specification of boundary conditions on the downstream edge of the flap is not clear, by construction, no grid lines originate there (this follows from equation 6). Consider the trailing edge of the flap shown magnified in Fig. 3-15). Based on the criteria for the first point away from the boundary (see beginning of this subsection), in general, $\Delta_u \neq$ flap thickness $\neq \Delta_l$. The y grid spacing is thus undesirably discontinuous at this section. To achieve continuity of the y-grid spacing at the flap trailing edge, the height of the upper surface (y_b) is modified from $y_b = 3.856$ to $y_b = 3.775$ cm. This corresponds to choosing $\Delta_u' =$ flap thickness $= \Delta_l' = \text{minimum}(\Delta_u, \Delta_l)$ where the primed quantities are the finally employed values. This approach leads to a reduction of 0.081 cm in the flap trailing edge thickness which is approximately 5 percent of the external boundary layer thickness. The value of β (see Fig. 3-3 (c)) changes from 18.65° to 19.16° . For a freestream Mach number, $M_\infty = 1.2$, a simple Prandtl Meyer expansion analysis indicates an acceptable variation in pressure (2.7%) and Mach number (1.0%). This is comparable to (or less than) the uncertainty introduced by the boundary layer displacement effect (since the initial boundary layer thickness is not known). The height H (= 6.8 cm) representing the height of the external flow above the flap at the upstream boundary is chosen to ensure that the Mach waves arising from the flap, after reflection from the outer boundary (due to the freestream boundary conditions applied), pass through the downstream boundary and do not pollute the computation in the region of interest.

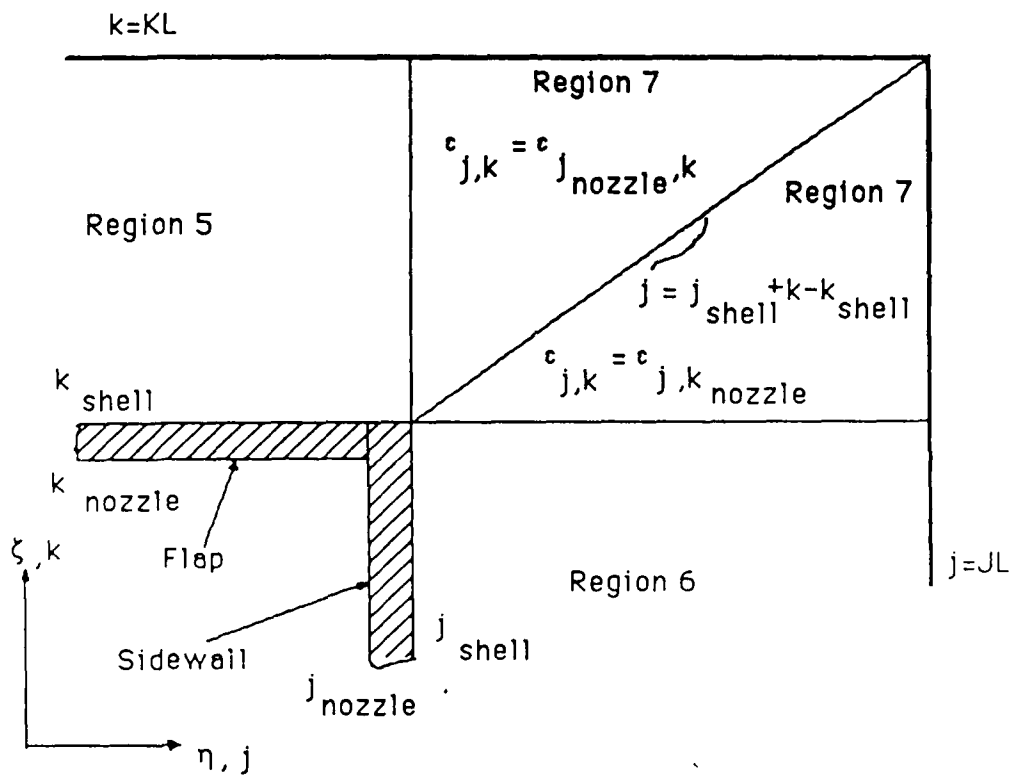


Figure 3-10: Implementation of Eddy Viscosity in Region 7

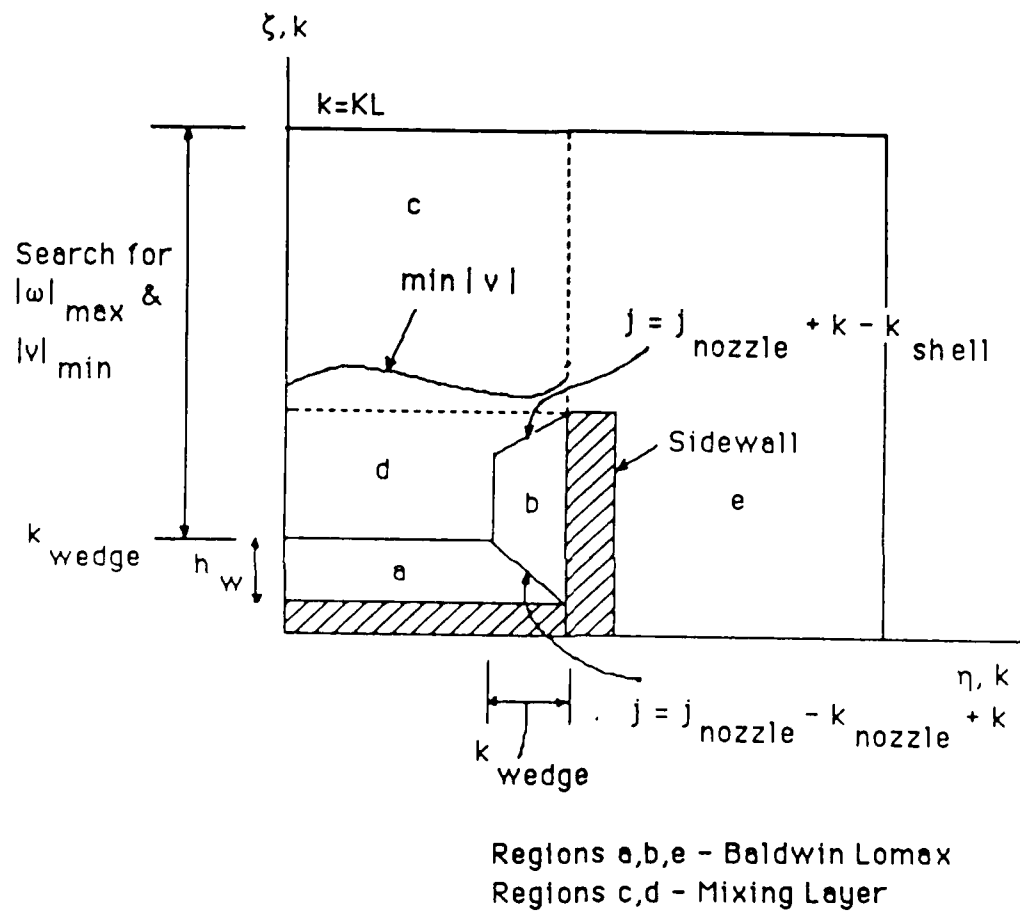
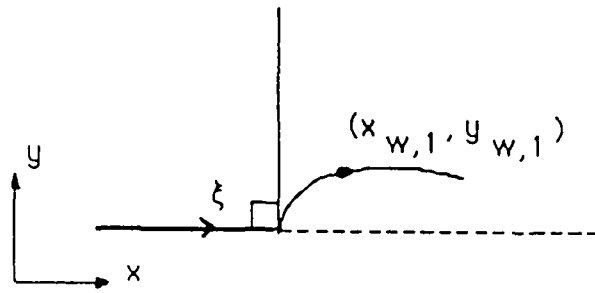
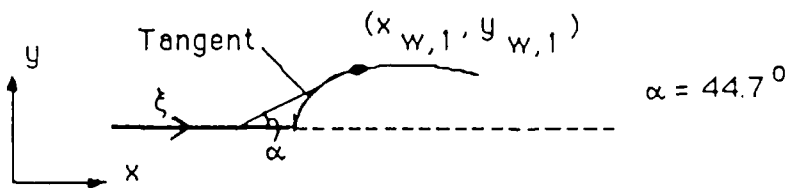


Figure 3-11: Interfacing of Eddy Viscosity Models at Type III Cross Section



a) Actual (Experiment)

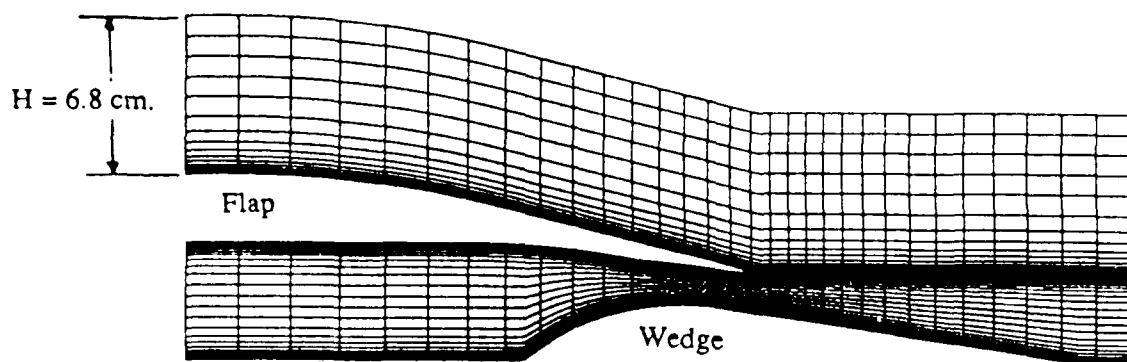


b) Modified (Computation)

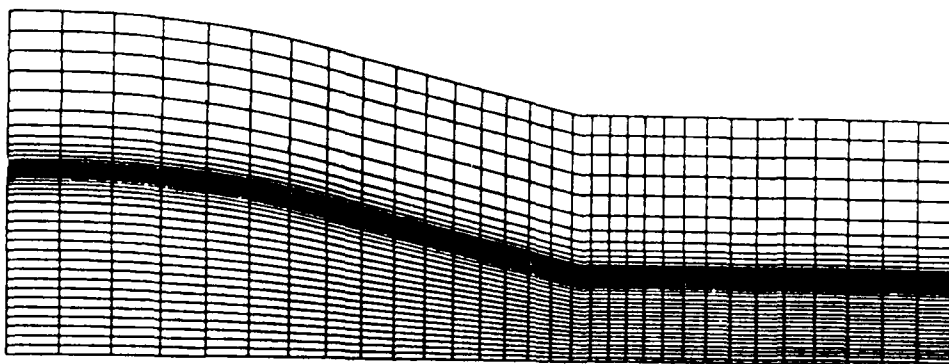
Figure 3-12: Modification of Wedge Leading Edge

In the internal flow region ($j < j_{nozzle}$, $k < k_{nozzle}$), the y grid is stretched to concentrate more points near the wedge and flap inner surfaces. In region 5, the y spacing is adjusted to concentrate grid points only at the flap outer surface. The y spacing in region 5 is extended to region 7. In region 6 ($j > j_{shell}$, $k < k_{shell}$), the grid is stretched away from $k = k_{shell}$ towards $k = 1$ ending in several equal spaced grid lines. The grid spacing at the junction of regions 6 and 7 varies in a smooth fashion.

3) Z (spanwise) grid spacing: Fig. 3-13 shows typical $j =$ constant planes of the grid. A total of 39 points are employed in the z direction ($J_L = 39$), with 21 (= J_{nozzle}) points in the



a) $j \leq j_{\text{nozzle}}$



b) $j \geq j_{\text{shell}}$

Figure 3-13: Grids in $j = \text{constant}$ planes

Table 3-3: X-locations (cm.)

Stn.	X(cm.)	Stn.	X(cm.)	Stn.	X(cm.)	Stn.	X(cm.)
1	140.1600	9	150.8829	17	157.2641	25	162.0490
2	141.7600	10	151.8758	18	157.8506	26	162.8323
3	143.3341	11	152.8056	19	158.3998	27	163.6783
4	144.8079	12	153.6761	20	158.9224	28	164.5920
5	146.1879	13	154.4911	21	159.4552	29	165.5790
6	147.4799	14	155.2542	22	160.0308	30	166.6244
7	148.6897	15	155.9688	23	160.6524	31	167.6698
8	149.8223	16	156.6377	24	161.3238	32	168.7153

interior nozzle flow. To obtain continuity of z-grid spacing adjacent to the wall, for reasons similar to those at the trailing edge of the flap, the sidewall exterior surface is assumed parallel to the x-axis i.e., the 4.75° inward slant is ignored. A Prandtl Meyer analysis similar to that carried out for the flap thickness indicates that the effects are modest. Uniformity is achieved by assuming that the sidewall thickness is arbitrarily small and equal to the value necessary for adequate resolution of the interior and exterior side boundary layers.

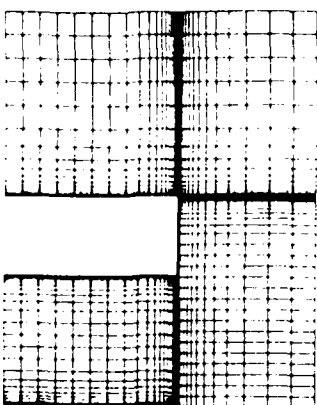
3.8. Initial and Boundary Conditions

The freestream and wall (temperature) conditions (from experiment) are summarized in Table 3-1. For the internal flow, the choice of nozzle pressure ratio (NPR = 2) is dictated by two factors:

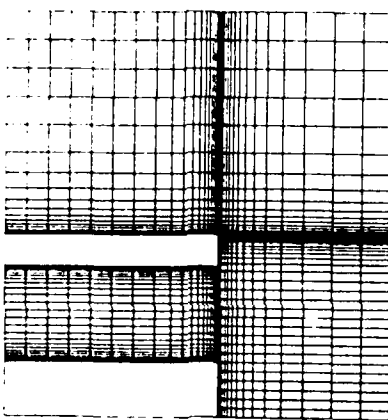
- throat is choked (NPR greater than 1.89), and
- shock must hit wedge as far upstream as possible to avoid separation from extending into the wake region where the mixing layer eddy viscosity model is employed.

The boundary conditions employed may be classified into the following types:

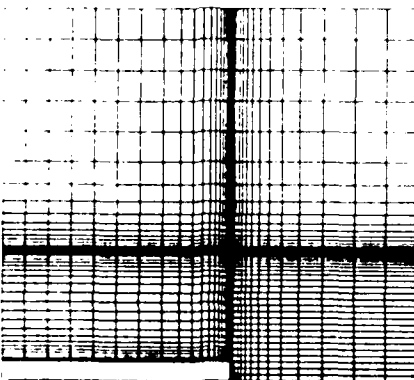
- Upstream boundary
- Downstream boundary



a) Type I



b) Type II



c) Type III

Figure 3-14: Grids in i - constant planes

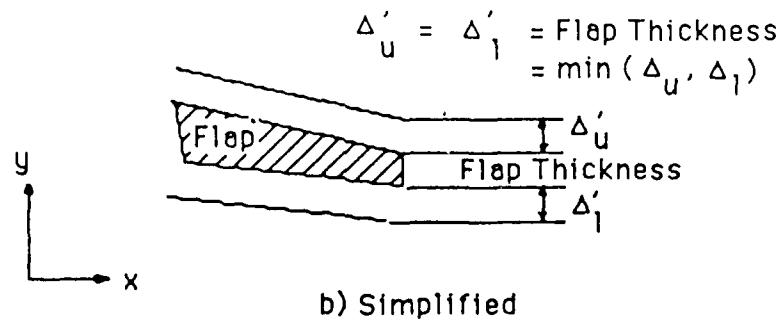
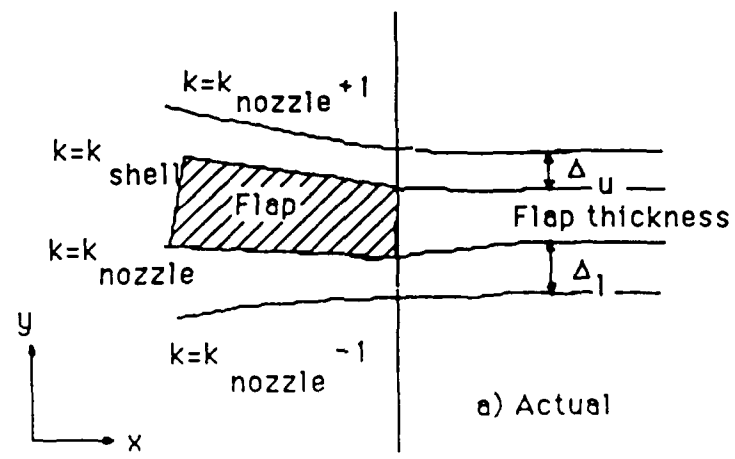


Figure 3-15: Modification at Trailing Edge of Flap

- Solid boundaries
- Symmetry boundaries
- Freestream Boundaries

Upstream (Inflow) Boundary: The upstream boundary profile may be classified into two regions: external flow and internal flow. In the external flow regions, the flow profiles in regions 5 and 6 are specified by assuming that the boundary layers (numbers 4 and 5 respectively) develop from the tip of the nozzle (Fig. 3-2). Under this assumption, the flow profile is generated separately with a 2-D compressible boundary layer code [55]. In region 7, the boundary layer profiles are combined in a manner similar to that employed for the eddy viscosity i.e., points below the dividing line in region 7 obtain the flow variable values from region 6 along $j = \text{constant}$ lines while points above the line obtain their values from region 5 along $k = \text{constant}$ lines.

In the internal flow region the specification of the boundary condition is somewhat more complex. The application may be divided into inviscid and viscous regions. In the inviscid region (where the flow is subsonic), from the theory of characteristics [62],

$$\frac{\partial p}{\partial t} = - (u - a) \frac{\partial p}{\partial x} \quad (21)$$

The values of pressure at the previous iteration permit the computation of the value of pressure at the next time-step using one-sided first-order accurate differences in space and time. Since the total mass flow rate depends upon the total pressure, total temperature and the throat area, ($w_t \sim P_t / \sqrt{T_t}$), the total pressure and total temperature are held fixed. In the inviscid region, the total pressure and the pressure (at timestep (n+1)) yield the Mach number (and hence the other flow parameters) at (n+1). In the viscous region, the velocity profile in the boundary layer may be obtained from the incompressible law of the wall/wake [63, 55], with $M_\infty \ll 1$

$$U = u_\infty \left(\frac{1}{k} \ln \left(\frac{y u_\infty}{v_w} \right) + B + \frac{2\pi}{\kappa} \sin^2 \left(\frac{\pi y}{2\delta} \right) \right) \quad (22)$$

In equation 22, u_* denotes the friction velocity (known since the magnitude of the wall shear stress is maintained fixed), B is a constant ($= 5.1$), Π is the wake strength parameter (see equation 24). The magnitude of the wall shear stress τ_w ($c_f = 6.1 \times 10^{-3}$ based on the nominal Mach number), the boundary layer thickness (δ) and total temperature (T_t) are maintained fixed. In the above formula therefore,

$$u_* = \sqrt{\tau_w / \rho_w} \quad (23)$$

$$\Pi = \frac{k}{2} \left(\frac{U_\infty^{k+1}}{u_*} - \frac{1}{k} \ln \left(\frac{\delta u_*}{v} \right) - B \right) \quad (24)$$

Equations 22 through 24 permit the determination of velocity u in the boundary layer. The temperature may then be computed with the formula :

$$T = T_t - \frac{1}{2C_p} u^2 \quad ; \quad v = w = 0 \quad (25)$$

The upstream boundary condition in the internal flow region therefore varies with the computation. We found this boundary condition quite satisfactory as is evident from results presented in subsection 3.11.

Downstream (Outflow) Boundary: The outgoing flow is supersonic, and the outflow boundary is essentially perpendicular to the outgoing flow. The flow characteristics therefore point from the inside of the computational domain to the outside, and thus the outflow boundary flow variables must be determined from the interior flow solution. The conventional zero-gradient extrapolation $\partial/\partial\xi = 0$ condition is employed. To prevent the effects of this boundary condition from affecting the region of interest, the computational domain is extended two ξ -planes downstream of the trailing edge of the wedge.

Solid boundaries: At a solid boundary, the following boundary conditions are applied

$$\begin{aligned} p \bar{v} &= 0 \\ \frac{\partial p}{\partial n} &= 0 \end{aligned} \quad (26)$$

$$T = T_w$$

where $\bar{v} = (u, v, w)$ is the Cartesian velocity vector, p is the static pressure, the direction n is

normal to the boundary and T_w is a specified wall temperature (see Table 3-1). The boundary condition for static pressure is an approximation to the exact boundary condition derivable from the normal component of the momentum equations, and has been successfully employed for a variety of flows exhibiting shock-boundary layer interaction [15, 22, 44, 64, 65]

Symmetry boundaries: On a symmetry boundary the following conditions apply :

$$\begin{aligned} \rho \bar{v} \cdot \hat{n} &= 0 \\ \frac{\partial}{\partial n} (\rho \bar{v} \times \hat{n}) &= 0 \\ \frac{\partial p}{\partial n} &= 0 \\ \frac{\partial T}{\partial n} &= 0 \end{aligned} \tag{27}$$

where \hat{n} is the direction normal to the symmetry boundary.

Freestream boundaries: At these boundaries, the flow variables are obtained from the conditions outlined in Table 3-1 and are applied in the form :

$$\begin{aligned} \rho &= \text{specified} \\ u &= \text{specified} \\ v = w &= 0 \\ \rho e &= \text{specified} \end{aligned} \tag{28}$$

Fig. 3-16 shows schematically the boundary conditions as applied at each of the three types of cross sections. In all computations described in this research, the flow initial condition is obtained by simply propagating the profiles at the upstream boundary ($\xi = 0$) to all downstream grid points.

3.9. Computational Details

The marching of the solution toward steady-state is carried out in many phases. For the first approximately $0.1 T_{c,\text{ext}}$ (characteristic time based on external flow - the time required for a fluid particle to travel from the upstream to the downstream end of the physical

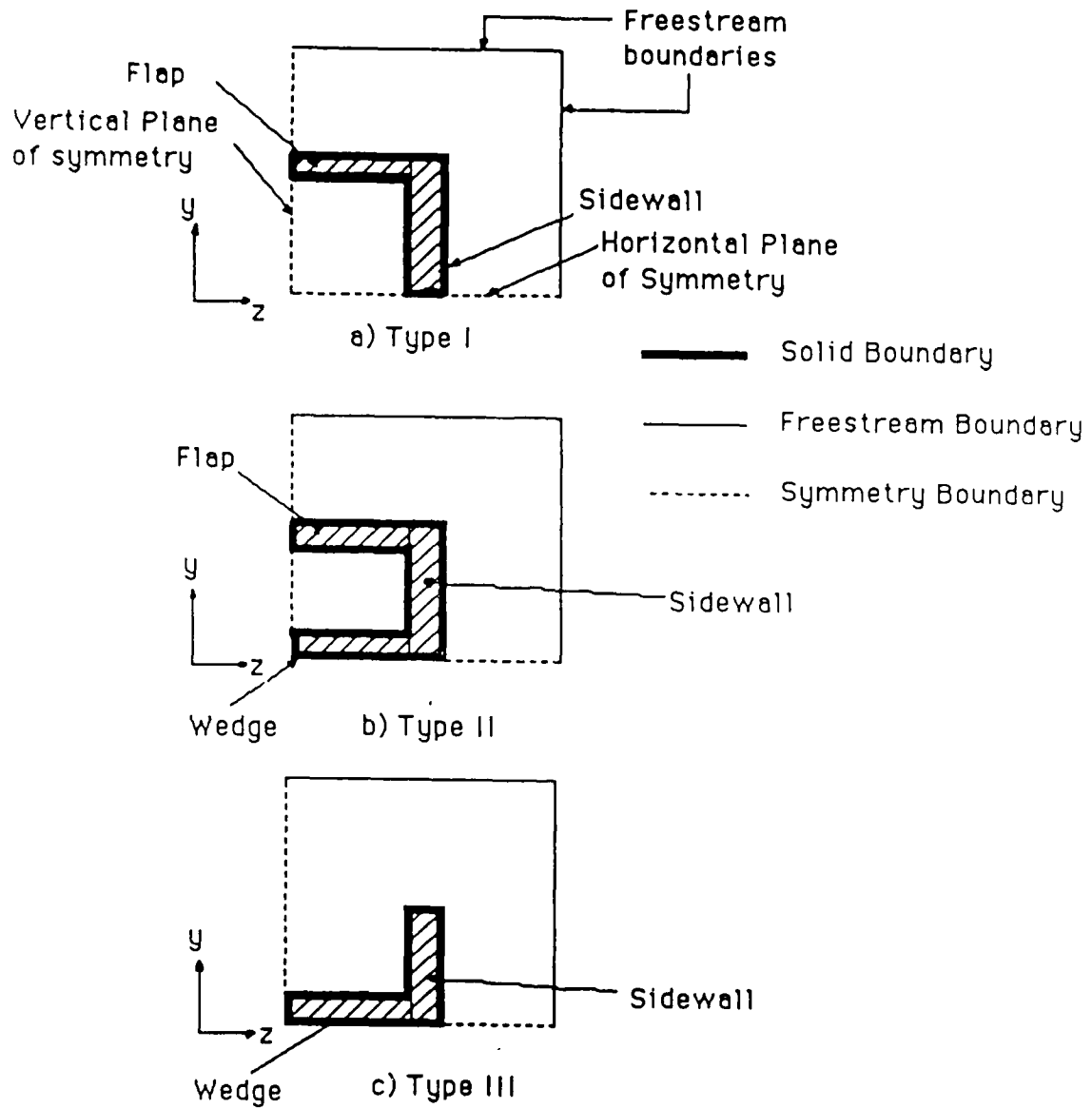


Figure 3-16: Boundary Conditions at Each Type of Section

domain in the external flow inviscid region), the sublayer solution is updated every explicit iteration. This is necessary because the initial condition is obtained by propagating the upstream boundary condition to all streamwise planes and is thus far removed from the steady-state solution. Therefore, the explicit solution develops quite rapidly and the sublayer solution must be updated every explicit step. In the initial stages also, a "transient damping procedure" is employed to prevent numerical instability of the hybrid algorithm. A "poor" initial guess often leads to transient spatial oscillations in static pressure. These oscillations disappear after approximately one characteristic time. To prevent these unphysical transient oscillations from adversely affecting the line sublayer, the transverse pressure gradient $\partial p / \partial y'$ in the line sublayer is set to zero for an initial time interval approximately equal to one $T_{c,ext}$. In the present instance, numerical instability is observed (originating at the external corner) when the transverse pressure gradient is switched on even after one $T_{c,ext}$. The problem is "solved" by computing this gradient normally at all points except near the external corner (see Fig. 3-17) where, over the last few grid points the value of the gradient is arbitrarily set to a value determined by a linear profile to obtain zero value at the corner. The effect of this assumption is not expected to be significant.

After about one characteristic time $T_{c,ext}$, the sublayer solution develops at a slower pace and, since the sublayer solution takes several times the CPU as the explicit solution, it is updated only once about every eight time steps and the solution marched to convergence.

Convergence is determined by checking flow variation over roughly one $T_{c,ext}$. Typically, the solution vector U (Eqn. 8) and the eddy viscosity ϵ are monitored on the ordinary grid, while the velocities, temperatures, their gradients and ϵ are monitored on the sublayer and corner grids. Since certain quantities (ϵ in the freestream for example) obtain very small values, relative changes in these may be rather large and misleading. Variations in all quantities are therefore monitored relative to local values as well as over global reference values to determine convergence. One interesting observation is that the convergence properties of the sublayer algorithm improve significantly when the eddy viscosity (in the

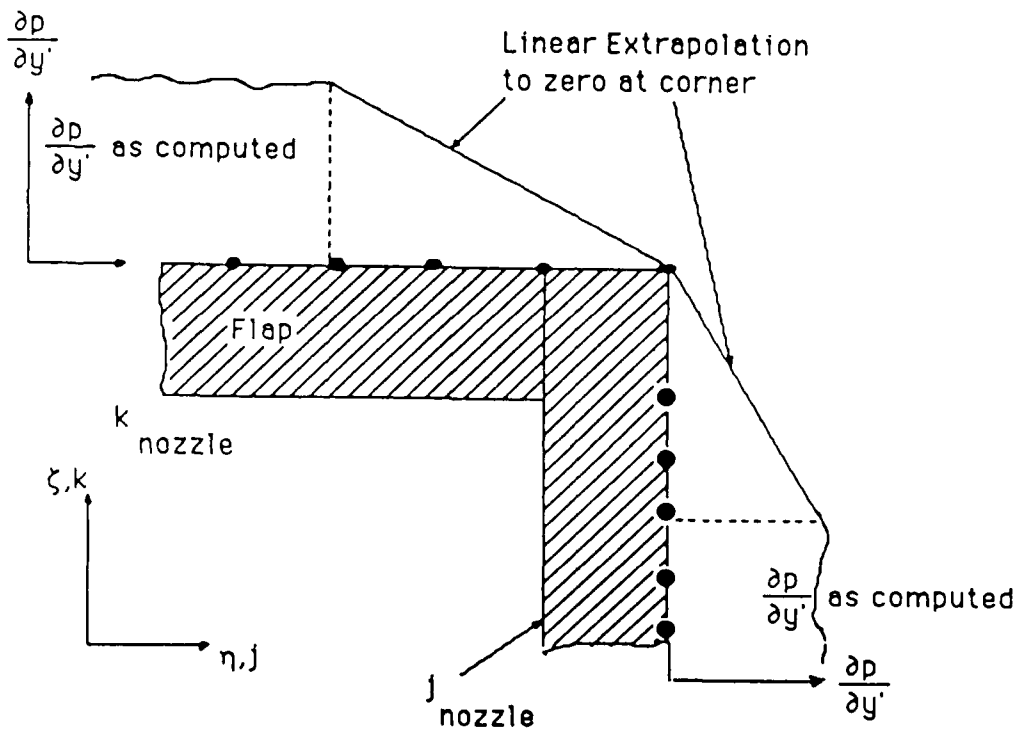


Figure 3-17: Computation of Transverse Pressure Gradient in Sublayer at External Corner

sublayer) is averaged over successive sublayer solutions. The cause of this is presently unclear. Convergence is achieved over most¹ parts of the domain by marching the explicit solution forward by approximately $4.10 T_{c,\text{ext}}$ flow development time corresponding to 1694 iterations on the ordinary grid. This requires roughly 13 hours CPU on the 2-pipe CYBER 205 at the John von Neumann Center (JVNC).

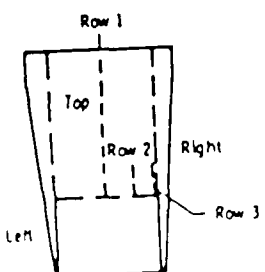
¹see subsection 3.11 regarding possible existence of pressure waves in the vicinity of the sidewall-wedge corner

3.10. Comparison with Experiment

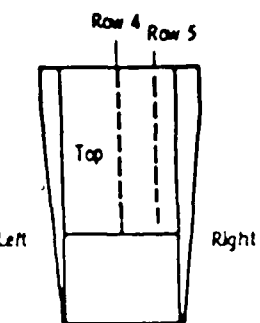
The accuracy of the numerical results are validated by comparison with experimental static-pressure data of Mason and Abeyounis [46]. The locations of the 14 rows of static pressure orifices in the experimental configuration are shown in Fig. 3-18 and summarized in Table 3-4. The computed flowfield is observed to converge to a steady state at all streamwise planes over a large spanwise (η) portion of the domain from the symmetry plane ABFE (Fig. 3-5) to a spanwise station near the sidewall. In the vicinity of the corner formed by the wedge and the sidewall, however, an unsteady solution is obtained as described in subsection 3.11. The experimental data includes mean surface pressure measurements only. Consequently, only the static pressure distributions on the centerlines of the flap (inner surface), flap (outer surface) and wedge are compared in the present report. These correspond to rows 1 (Fig. 3-18 (a)), 4 (Fig. 3-18 (b)) and 10 (Fig. 3-18 (e)) respectively. In the following graphs, the static pressure is non-dimensionalized with the total pressure in the nozzle at the upstream station and the dimension d , the maximum height of the model (Fig. 3-3) is employed to normalize the axial distance x .

The pressure along the wedge centerline is plotted in Fig. 3-19. As observed in experiment, the flow expands as the flap trailing edge ($x/d = 1.0$) is reached. Downstream of the flap trailing edge (nozzle exit), the static pressure rises somewhat abruptly indicating the possible presence of a shock on the surface of the wedge. Beyond this pressure rise ($x/d > 1.15$), experimental observations indicate a roughly constant static pressure profile. From Fig. 3-19, the computations overpredict the static pressure downstream of the wedge shock by approximately 5 percent. The conclusion made by the experimental investigators regarding the existence of flow separation on the wedge (beyond the shock) is to be confirmed with particle tracing techniques (subsection 3.11).

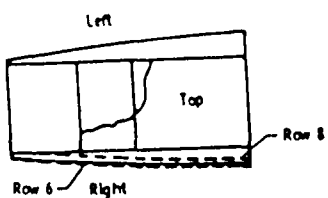
The pressure along the flap internal centerline is plotted in Fig. 3-20. Note that the last experimental station is located at roughly $x/d = 1.0$ which corresponds to the flap trailing edge. The pressure drops as the flap trailing edge is reached. The calculated and experimental static pressures are in good agreement over the entire length of the flap. The



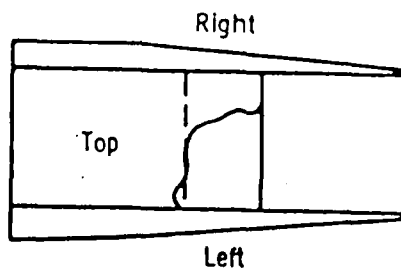
(a) Internal flap pressure orifices.



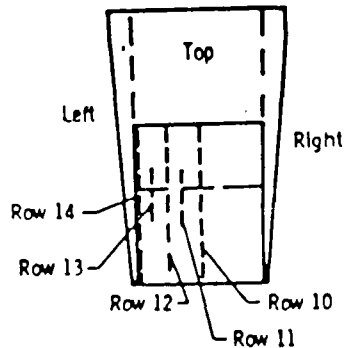
(b) External flap pressure orifices.



(c) External sidewall (right sidewall)
pressure orifices.



(d) Internal sidewall (left sidewall)
pressure orifices.



(e) Wedge pressure orifices.

**Figure 3-18: Location of Experimental Static Pressure Orifices.
From [46]**

Table 3-4: Summary of Static Pressure Orifice Locations

Row #	Location	Figure
1,2,3	Internal Flap	3-18 (a)
4,5	External Flap	3-18 (b)
6,7,8	External Sidewall	3-18 (c)
9	Internal Sidewall	3-18 (d)
10-14	Wedge	3-18 (e)

assumption made on the flap trailing edge thickness apparently did not affect the computations.

The pressure coefficient along the flap external centerline is plotted in Fig. 3-21. The comparison shows reasonable agreement for $x/d < 0.45$. For values of $x/d > 0.45$ however, the computed pressure coefficient is somewhat higher than observed in experiment. The cause of this discrepancy is under investigation. For the low-expansion-ratio configuration, the experimental static pressure shows spanwise variation beyond the nozzle ($x/d \geq 0.8$) on the flap outer surface [46] and further comparison is necessary.

3.11. Analysis of Computed Flow Field Structure

One of the many advantages of numerical simulation of flow fields is the capability of complete analysis. In particular, it is perhaps easier to detect the existence of critical flow structures leading to a more complete understanding of the salient features of flows where experimental visualization is difficult.

Three-dimensional computations as described above necessarily result in sizeable datasets. The processing of such large sets of numbers is a non-trivial task and, for the current computation, is currently under progress. The primary focus of the flow field analysis is on the study of particle traces generated with the computed flow field. In the present instance, it is proposed to employ a 3-D particle tracing code [66]. A number of particles are released in different parts of the domain and their motion is studied to detect coherent flow structures such as vortices and regions of separation. It is proposed to analyze the paths of these particles with sophisticated color graphics software

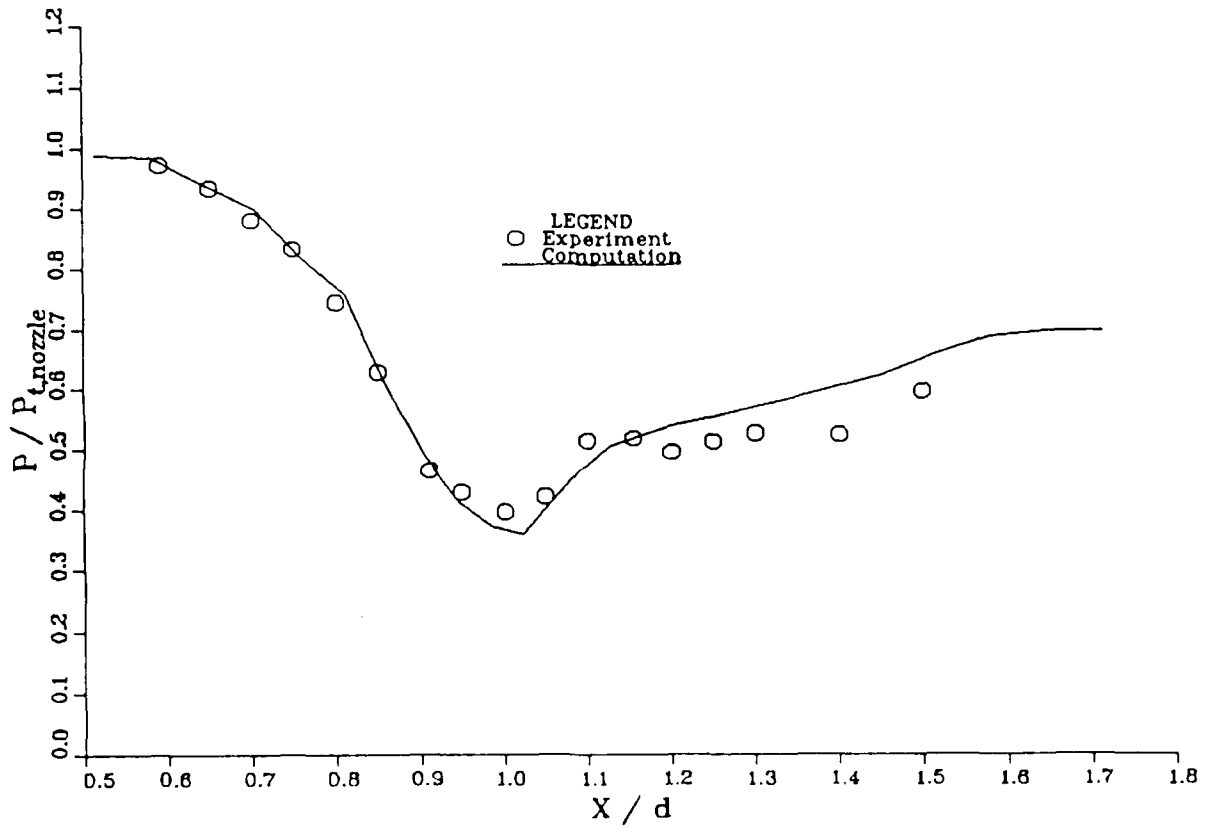


Figure 3-19: Static Pressure Variation on Wedge Centerline - Comparison with Experiment

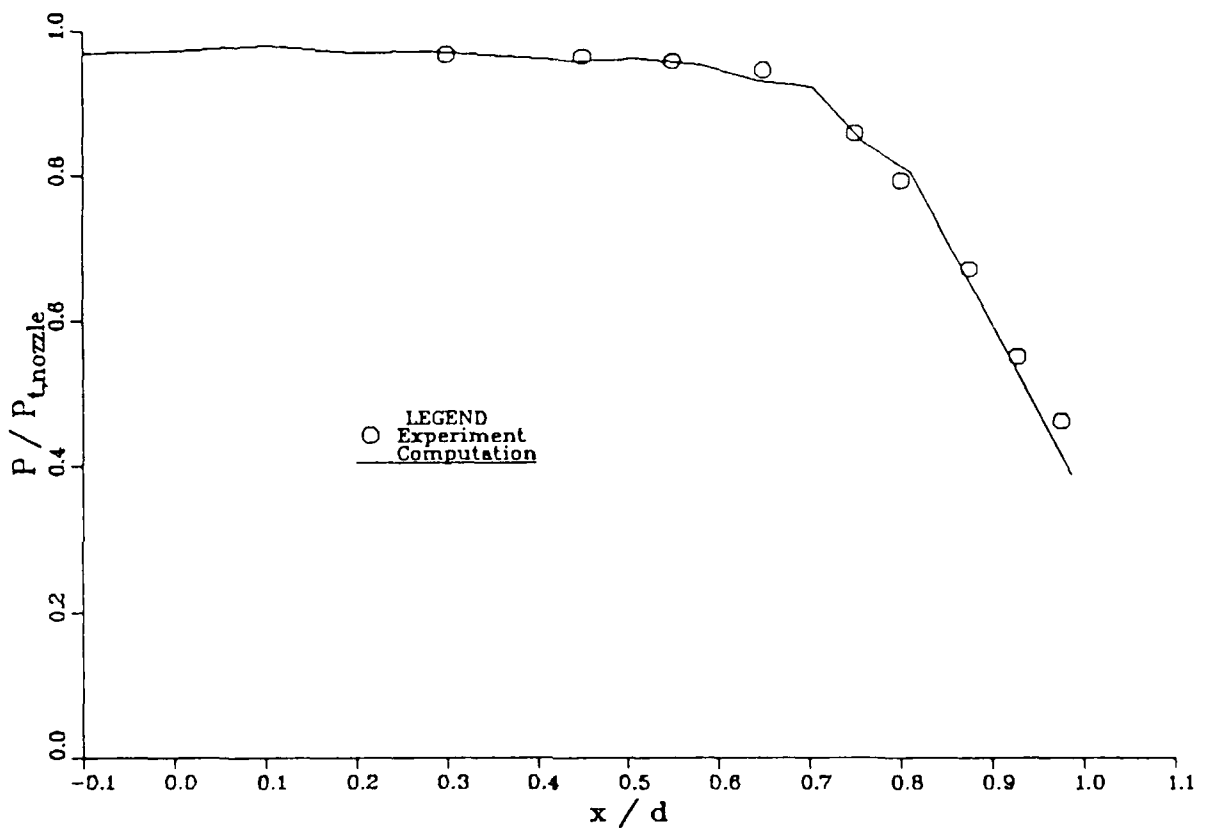


Figure 3-20: Static Pressure Variation on Flap Inner Centerline - Comparison with Experiment

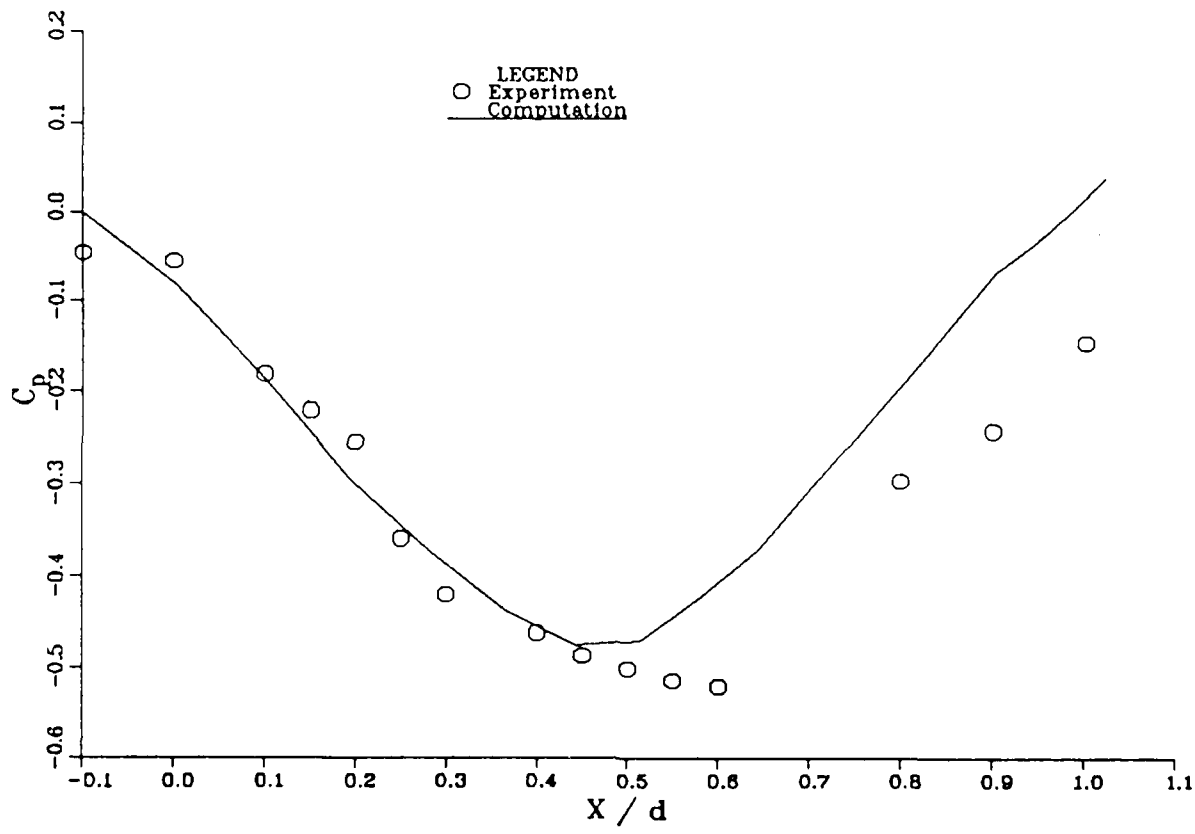


Figure 3-21: Static Pressure Variation on Flap Outer Centerline - Comparison with Experiment

(MOVIE.BYU) to provide a proper perspective.

An indication of the appropriateness of the upstream boundary condition for internal flow is obtained from Fig. 3-22 where the upstream static pressure is plotted against the number of iterations. The pressure displays oscillatory behavior as the solution develops. The amplitude of these oscillations is quite small (~ 0.3 %). These oscillations persist even at "steady state" conditions and do not affect the flow solution to any significant extent insofar as the surface pressures are concerned.

Preliminary analysis of the results indicates the existence of pressure waves at sidewall-wedge corner where an unsteady solution is observed. This conclusion is supported by Fig. 3-23 which shows the development of pressure along an axial line on the wedge surface near the wedge-sidewall corner. The peaks marked A,B and C in Fig. 3-23 demonstrate the existence of a pressure wave. It is not clear now if these are actual physical phenomena or if they are consequences of the numerical solution process (for example due to the downstream boundary conditions). The phenomenon is being analyzed further.

Deductions from values of shear stresses also point to the existence of regions of separated flow on the wedge ($x/d \sim 1.0$). Separation is also indicated on the external corner formed by the flap and the sidewall though it is not clear now if this is due to the assumptions regarding the geometry of the nozzle sidewall.

3.12. Conclusion

Preliminary results of a complex nozzle flow simulation indicate very good agreement between theory and experiment along the centerline of the nozzle. Modest discrepancies are observed on the flap external centerline. The flow seems rather complex with the existence of a pressure wave system in the wedge-sidewall corner. As indicated above, we expect further analysis of the computed flow field to result in the detection of further coherent structures. Thus we should have a better understanding of the flow dynamics.

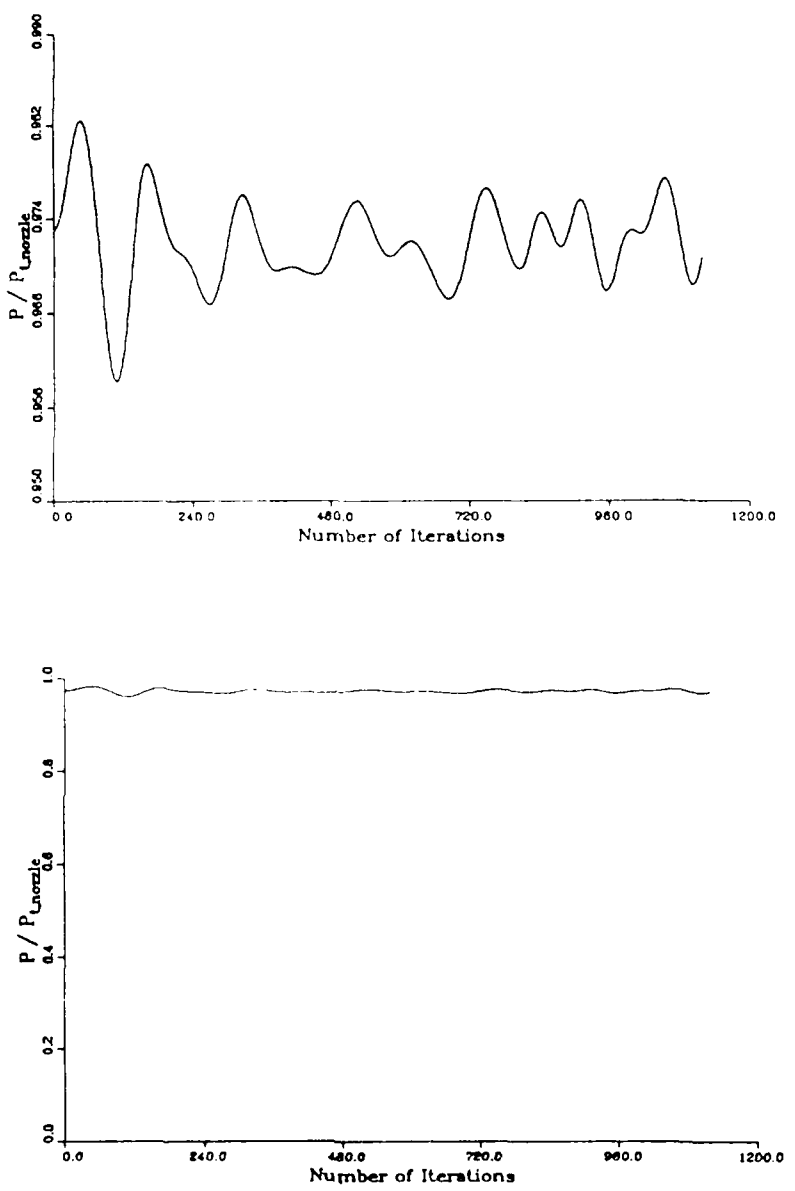


Figure 3-22: Development of Static Pressure at Upstream Internal Flow Boundary

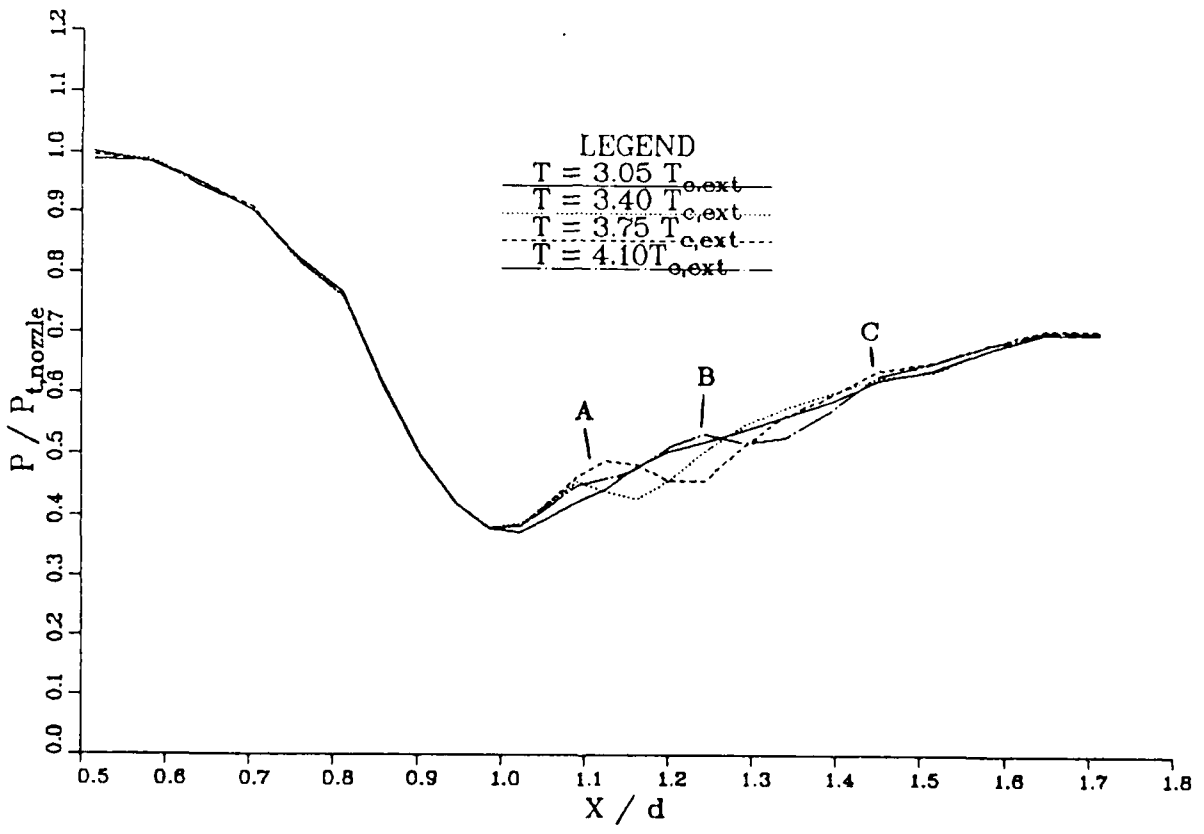


Figure 3-23: Static Pressure Near Sidewall-Wedge Corner

4. Conclusion and Future Work

A three-dimensional graphics based interactive method of grid generation is developed. The approach employs two phases. In the first phase, the algebraic multisurface technique of Eiseman is utilized, together with the precise point distribution technique of Smith *et al.* In the second phase, a series of direct grid modification techniques are utilized to meet specific grid requirements not easily satisfied during the first phase. The generality of the method is demonstrated for a twin-jet axisymmetric nozzle and an aircraft section.

A code based on the hybrid explicit-implicit algorithm [47] is modified in this research to compute nozzle flows. The principal modifications include the ability to simulate flow fields for geometries with internal and external flows and the use of the mixing layer model where these flows meet. The modifications retain the vectorization philosophy of the original code. The major coding modifications involve the solution of the sublayer equations on a larger number of surfaces as a result of the more complex nozzle topology (as compared to the 3-D sharp fin topology for example) and the interfacing of the two different eddy viscosity models employed.

The flow in two non-axisymmetric nozzles is computed under the assumptions of horizontal and vertical symmetry. The freestream Mach number of the external flow is 1.2 and the nozzle pressure of the internal flow is 2.0. One salient feature of the computation is the employment of a different upstream boundary condition for the internal flow. This condition depends upon the theory of characteristics for inviscid regions and the law of the wall/wake for the viscous regions.

The solution for the flow field on the centerline is converged. Comparison of static pressure values at the flap (inner and outer) and wedge surface centerlines with the experimental observations of Mason and Abeyounis [46] indicate very good agreement with modest discrepancies in the shear layer region where the computations predict generally higher pressures.

A preliminary analysis of the computed flow field indicates the existence of a shock wave

on the wedge in the region beyond the flap trailing edge. The solution in the corner formed by the wedge and the sidewall displays unsteady behaviour (Fig. 3-23). The wave structure of the flow in this region may not have been detected in the experiment due to inadequate frequency response characteristics of the experimental apparatus.

Future work will focus on a more thorough analysis of the unsteady phenomenon discussed above. It is envisaged that the flow will be studied in detail with numerical particle tracing techniques and color graphics to identify important flow structures such as areas of separation and vortices. A refined case with more (64) axial planes is also under consideration.

References

- [1] Hunt, B., Surber, L., and Grant, G.
Propulsion-System Integration for Tactical Aircraft.
Aeronautics and Astronautics 18(6):62 ff., 1980.
- [2] Capone, F., Hunter, B., and Poth, G.
Subsonic/Supersonic Nonvector Aero-propulsive characteristics of
Nonaxisymmetric Nozzles Installed on an F-18 Model.
AIAA Paper 81-1445, 1981.
- [3] Doonan, J., Callahan, C., and Bowers, D.
High Speed Wind Tunnel Test Evaluation of STOL Dedicated Advanced Nozzle
Concepts.
AIAA Paper 83-1225, 1983.
- [4] McLafferty, G., and Peterson, J.
Results of a Rectangular Vectoring Reversing Nozzle on an F100 Engine.
AIAA Paper 83-1285, 1983.
- [5] Hakim, A., Arena, A., and Obye, R.
Axisymmetric Approach and Landing Thrust Reverser Concepts: Static
Performance Test Results.
AIAA Paper 83-1227, 1983.
- [6] Speir, D., and Blozy, J.
Development of Exhaust Nozzle Internal Performance Prediction Techniques for
Advanced Aircraft Applications.
AIAA Paper 81-1490, 1981.
- [7] Nelson, D., and Bresnahan, D.
Ejector Nozzle Test Results at Simulated Flight Conditions for an Advanced
Supersonic Transport Propulsion System.
AIAA Paper 83-1287, 1983.
- [8] Straight, D.
Effects of Shocks on Film Cooling of a Full Scale Turbojet Exhaust Nozzle Having
an External Expansion Surface.
AIAA Paper 79-1170, 1979.
- [9] Robinson, C., and High, M.
*Exhaust Plume Temperature Effects on Nozzle Afterbody Performance Over the
Transonic Mach Number Range*.
Technical Report, AEDC TR-74-9, 1974.
- [10] Mace, J., and Cosner, R.
Analysis of Viscous Transonic Flow Over Aircraft Forebodies and Afterbodies.
AIAA Paper 83-1366, 1983.
- [11] Swanson, R.
Navier-Stokes Solutions for Nonaxisymmetric Nozzle Flows.
AIAA Paper 81-1217, 1981.
- [12] Krishnamurty, K.
Acoustic Radiation from Two-Dimensional Rectangular Cutouts in Aerodynamic
Surfaces.
NACA TN 3487, 1955.

- [13] Hankey, W., and Shang, J.
Analyses of Pressure Oscillations in an Open Cavity.
AIAA J. 18:892-898, 1980.
- [14] Hankey, W., and Hunter, L., and Harney, D.
Self-Sustained Oscillations (Buzz) on Spiked Tip Bodies.
AFFDL-TM-79-23-FXM, AF Flight Dynamics Laboratory , 1979.
- [15] Shang, J., Smith, R., and Hankey, W.
Flow Oscillations of Spike-Tipped Bodies.
AIAA J. 20:25-26, 1982.
- [16] Dusa, D., Speir, D., Rowe, R., and Leavitt, L.
Advanced Technology Exhaust Nozzle Development.
AIAA Paper 83-1286 , 1983.
- [17] Berrier, B., and Mason, M.
A Static Investigation of Yaw Vwctoring Concepts on Two-Dimensional
Convergent-Divergent Nozzles.
AIAA Paper 83-1288 , 1983.
- [18] Leavitt, L.
Effects of Various Empennage Parameters on the Aerodynamics Characteristics of
a Twin-Engine Afterbody Model.
AIAA Paper 83-0085 , 1985.
- [19] Smith, R.
Numerical Solution of the Navier-Stokes Equations for a Family of Three-
Dimensional Geometries.
AIAA Paper 80-1349 , 1980.
- [20] Steger, J., and Bailey, H.
Calculation of Transonic Aileron Buzz.
AIAA J. 18:249-255, 1980.
- [21] Knight, D.
*Research to Develop a Fully Three-Dimensional Navier-Stokes Code for High
Speed Inlets.*
Air Force Contract F33615-78-C-3008, Wright-Paterson AFB, OH, AFOSR, Bolling
AFB, DC, April, 1983.
- [22] Kumar, A.
Three-Dimensional Inviscid Analysis of the Scramjet Inlet Flow Field.
AIAA Paper 82-0060 , 1982.
- [23] MacCormack, R.,
A Numerical Method for Solving the Equations of Compressible Viscous Flow.
AIAA J. 20:1275-1281, 1982.
- [24] Shang, J., and MacCormack, R.
Flow Over a Biconic Configuration with Afterbody Compression Flap - A
Comparative Numerical Study.
AIAA Paper 83-1668 , 1983.
- [25] Warming, R., and Beam, R.
On the Construction and Application of Implicit Factored Schemes for Conservation
Laws.
SIAM-AMS Proceedings 11:85-129, 1978.

- [26] Briley, R., and McDonald, H.
Solution of the Multi-Dimensional Compressible Navier-Stokes Equations by a Generalized Implicit Method.
J. Comp. Phys. 24:372, 1977.
- [27] Bardina, J., and Lombard, C.
Three-Dimensional CSCM Method for the Compressible Navier-Stokes Equations with Application to a Multi-Nozzle Exhaust Flowfield.
AIAA Paper 85-1193, 1985.
- [28] Dash, S., Wolf, D., and Sinha, N.
Parabolized Navier-Stokes Analysis of Three-Dimensional Supersonic and Subsonic Jet Mixing Problems.
AIAA Paper 84-1525, 1984.
- [29] Paynter, G.
Current Status of Inlet Flow Prediction Methods.
In *12th U.S. Navy Symposium on Aeroballistics*. David Taylor Naval Ship Research and Development Center, Bethesda, MD, May, 1981.
- [30] Mikhail, A., Hankey, W., and Shang, J.
Computation of a Supersonic Flow Past an Axisymmetric Nozzle Boattail with Jet Exhaust.
AIAA J. 18:869-875, 1980.
- [31] Hansen, J.
Navier-Stokes Solutions for an Axisymmetric Nozzle.
AIAA Paper 81-1471, 1981.
- [32] Cline, M., and Wilmoth, R.
Computation of High Reynolds Number Internal/External Flows.
AIAA J. 21:172-173, 1983.
- [33] Perry, K.
Non-Axisymmetric Nozzle/Aftbody Flow Fields Analysis.
Technical Report, AFWAL-TR-81-3046, 1981.
- [34] Shang, J.
Oscillatory Compressible Flow Around a Cylinder.
AIAA Paper 82-0098, 1982.
- [35] Levy, L.
Experimental and Computational Steady and Unsteady Transonic Flows about a Thick Airfoil.
AIAA J. 16:564-572, 1978.
- [36] Thompson, J., and Warsi, Z.
Boundary Fitted Coordinate Systems for Numerical Solution of Partial Differential Equations - A Review.
J. Comp. Phys. 47:1-108, 1982.
- [37] Thompson, J.F.
A Survey of Grid Generation Techniques in Computational Fluid Dynamics.
AIAA Paper 83-0447, 1983.

- [38] Ives, D.C.
 Conformal Grid Generation.
 In J.F. Thompson (editor), *Numerical Grid Generation*, pages 107-136. North-Holland, New York, April, 1982.
- [39] Eiseman, P.R. and Smith, R.E.
 Mesh Generation Using Algebraic Techniques.
 In *Numerical Grid Generation Techniques*, NASA 2166, pages 73-120. October, 1980.
- [40] Thompson, J.F.
 General Curvilinear Coordinate Systems.
 In J.F. Thompson (editor), *Numerical Grid Generation*, pages 1-30. North-Holland, New York, April, 1982.
- [41] Thompson, J.F. and Warsi, Z.U.A.
 Boundary-Fitted Coordinate Systems for Numerical Solution of Partial Differential Equations - A Review.
J. Comp. Physics 47:1-108, 1982.
- [42] Smith, R.E., Kudlinski, R.A. and Everton, E.L.
 A Grid Spacing Control Technique for Algebraic Grid Generation Methods.
AIAA Paper 82-0226, 1982.
- [43] MacCormack, R.
Numerical Solution of the Interaction of a Shock Wave with a Laminar Boundary Layer.
 Lecture Notes in Physics, Vol. 8 Springer-Verlag, pp. 151-163, 1971.
- [44] Knight, D.D.
 A Hybrid Explicit-Implicit Numerical Algorithm for the Three-Dimensional Compressible Navier-Stokes Equations.
AIAA Journal 22(8):1056-1063, August, 1984.
- [45] Gaitonde, D.
 Three-Dimensional Interactive Grid Generation.
 Master's thesis, Rutgers University, 1986.
- [46] Mason, M., and Abeyounis, W.
Experimental Investigation of Two Nonaxisymmetric Wedge Nozzles at Free-Stream Mach Numbers up to 1.20.
 Technical Report, NASA Technical Paper 2054, Langley Research Center, Hampton, Virginia, 1982.
- [47] Knight, D.
A Vectorized Three-Dimensional Navier-Stokes Code for High Speed Inlets.
 Technical Report RU-TR-161-MAE-F, Rutgers University, New Brunswick, New Jersey, 1983.
- [48] Rubesin, M., and Rose, W.
 The Turbulent Mean-Flow, Reynolds-Stress and Heat-Flux Equations in Mass Averaged Dependent Variables.
NASA TMX 62248, March, 1973.
- [49] Pulliam, T., and Steger, J.
 Implicit Finite-Difference Simulations of Three-Dimensional Compressible Flow.
AIAA J. 18:159-167, 1980.

- [50] Keller, H.
Accurate Difference Methods for Nonlinear Two-Point Boundary Value Problems.
Siam J. Numerical Analysis 11:305-320, 1974.
- [51] Baldwin, B. and Lomax, H.
Thin Layer Approximation and Algebraic Model for Separated Flows.
AIAA Paper 78-257, 1978.
- [52] Buleev, N.
Theoretical Model of the Mechanism of Turbulent Exchange in Fluid Flows.
Technical Report 957, AERE, Hartnell, England, 1963.
- [53] Gessner, F., and Po, J.
A Reynolds Stress for Turbulent Corner Flows - Part III: Comparisons Between Theory and Experiment.
J. Fluids Engr., Trans. of ASME 98(22):269-277, 1976.
- [54] Steger, J. and Sorenson, R.
Automatic Mesh-Point Clustering Near a Boundary in Grid Generation with Elliptic Partial Differential Equations.
J. Comp. Physics 33:405-410, 1979.
- [55] York, B.
Evaluation of the Baldwin-Lomax Turbulence Model for a Class of Boundary Layer Flows.
Master's thesis, Rutgers University, 1984.
- [56] Thomas, P.
Numerical Method for Predicting the Flow Characteristics and Performance of Nonaxisymmetric Nozzles - Applications.
Technical Report, NASA CR-3147, 1980.
- [57] Baldwin, B., and MacCormack, R.
A Numerical Method for Solving the Navier-Stokes Equations with Application to Shock-Boundary Layer Interactions.
AIAA Paper 75-1, 1975.
- [58] Knight, D.D.
Calculation of a Simulated 3-D High Speed Inlet using the Navier-Stokes Equations.
AIAA Paper 83-1165, 1983.
- [59] Knight, D., Horstman, C., Shapey, B. and Bogdonoff, S.
The Flowfield Structure of the 3-D Shock Wave - Boundary Layer Interaction Generated by a 20 Deg. Sharp Fin at Mach 3.
AIAA Paper 86-0343; to appear, AIAA Journal, 1986.
- [60] Knight, D., Horstman, C., Ruderich, R., Mao, M-F. and Bogdonoff, S.
Supersonic Turbulent Flow Past a 3-D Swept Compression Corner at Mach 3.
AIAA Paper 87-0551, 1987.
- [61] Horstman, C. and Hung, C.
Computation of Three-Dimensional Turbulent Separated Flows at Supersonic Speeds.
AIAA Paper 79-0002, 1979.

- [62] Liepmann, H., and Roshko, A.
Elements of Gasdynamics.
John Wiley & Sons, Inc., New York, 1956.
- [63] Sun, C-C., and Childs, M.
A Modified Wall-Wake Velocity Profile for Turbulent Compressible Boundary Layers.
J. Aircraft 10(4), 1973.
- [64] Deiwert, G.
Numerical Simulation of High Reynolds Number Transonic Flows.
AIAA J. 13:1354-1359, 1975.
- [65] Kutler, P., Chakravarthy, S., and Lombard, C.
Supersonic Flow Over Ablated Nosetips Using an Unsteady Numerical Procedure.
AIAA Paper 78-213, 1978.
- [66] Raufer, D.
The Development of a 3-D Particle Tracing Algorithm and its Application to the Study of Swept Compression Corner Boundary Layer Interactions.
Master's thesis, Rutgers University, December, 1987.

Nomenclature

Symbols relevant to the geometric configuration in the experiment are provided in Fig. 3-3.

A_k	Reciprocal of G_k (Equation 1)
B-L	Baldwin Lomax turbulent eddy viscosity model
C_p	Specific heat at constant pressure
C_v	Specific heat at constant volume
C_{cp}	Turbulence model (B-L) constant (Equation 11)
C_{kleb}	Turbulence model (B-L) constant (Equation 14)
C_{mix}	Turbulence model (mixing layer) constant ($= 0.13$) (Equation 16)
c_p	Pressure coefficient
D	van Driest damping factor (Equation 10)
e	Total energy per unit mass
e_i	Internal energy per unit mass
F	Flux vector in ξ direction (Equation 7)
F_{Kleb}	Klebanoff intermittency function (Equation 11)
F_{max}	Velocity scale in outer turbulence model (Equation 12)
F_{outer}	Outer function in outer turbulence model (Equation 13)
F_{wake}	Wake function in outer turbulence model (Equation 12)
G	Flux vector in η direction (Equation 7)
H	Flux vector in ζ direction (Equation 7)
G_k	Integrals of interpolants ψ (Equation 1)
i	Index in the ξ direction
J	Jacobian of transformation (Equation 9)
j	Index in the η direction
k	Index in the ζ direction; thermal conductivity;
j_{nozzle}	j (spanwise) index corresponding to sidewall inner surface
j_{shell}	j index corresponding to sidewall outer surface
k	Constant in outer eddy viscosity formulation
k_{nozzle}	k index corresponding to flap inner surface

k_{shell}	k index corresponding to flap outer surface
l	Buleev length scale(B-L) (Equation 10); length scale (mixing layer - Equation 15)
M_{∞}	Freestream Mach Number (Table 3-1)
N	Total number of surfaces in multisurface technique (Equation 1)
N.P.R.	Nozzle Pressure Ratio (Table 3-1)
N_{Re}	Reynolds number (Table 3-1)
\hat{n}	Unit normal at surface (points inwards)
P	General multisurface transformation (Equation 1)
P_i	Parameterized surfaces (Equation 1)
P_t	Average tunnel total pressure (Table 3-1)
\Pr	Molecular Prandtl number
\Pr_t	Turbulent Prandtl number
p	Static pressure
R	Gas constant for air
r	Spanning variable in multisurface technique (Equation 1)
S.M.	Skewness measure (Equation 5)
T	Static temperature
T_c	Characteristic time
$T_{c,\text{ext}}$	Characteristic time based on external flow
$T_{t,t}$	Tunnel total temperature (Table 3-1)
$T_{t,j}$	Average jet total temperature (Table 3-1)
T_w	Wall temperature (Table 3-1)
t	Time
t_c	Characteristic velocity of mean flow (Equation 19)
t_{diff}	Characteristic turbulent diffusion time across sublayer (Equation 18)
t_{mean}	Time scale of unsteady mean motion
U	Solution vector $\langle \rho, \rho u, \rho v, \rho w, \rho e \rangle$ (Eqn. 8)
v	Velocity vector (u, v, w)
u	Cartesian velocity in x direction

u .	Friction velocity (Equation 23)
v	Cartesian velocity in y direction
$ v_{max} $	Magnitude of maximum velocity (mixing layer) (Equation 17)
$ v_{min} $	Magnitude of minimum velocity (mixing layer)(Equation 17)
w	Cartesian velocity in z direction
w_i	Theoretical mass flow rate in nozzle
x	Axis in the general streamwise direction
y	Axis normal to the horizontal plane of symmetry
z	Axis in the general spanwise direction
z'	Local sublayer distance normal to surface
z_m, z_m'	Height of computational sublayer
z_m^+	Sublayer height in wall units (non-dimensional)

GREEK SYMBOLS

Δ_l	Maximum permissible sublayer height on flap lower surface (Fig. 3-15)
Δ_u	Maximum permissible sublayer height on flap upper surface (Fig. 3-15)
Δ'_l	Actual sublayer height employed on flap lower surface (Fig. 3-15)
Δ'_u	Actual sublayer height employed on flap upper surface (Fig. 3-15)
δ	Boundary layer thickness
$\delta_1, \delta_{\text{flap inner}}$	Inner flap δ (Table 3-2)
$\delta_2, \delta_{\text{sidewall inner}}$	Inner sidewall δ (Table 3-2)
$\delta_3, \delta_{\text{wedge}}$	Wedge δ (Table 3-2)
$\delta_4, \delta_{\text{flap outer}}$	Outer flap δ (Table 3-2)
$\delta_5, \delta_{\text{sidewall outer}}$	Outer sidewall δ (Table 3-2)
ϵ	Eddy viscosity
ϵ_i	Inner eddy viscosity (Equation 10)
ϵ_o	Outer eddy viscosity (Equation 11)
ϵ_r	Characteristic eddy viscosity in sublayer (Equation 18)
η	Computational axis (index - j)

κ	von Karman constant ($= 0.4$) (Equation 10)
μ	Molecular dynamic viscosity
μ_T	Characteristic molecular dynamic viscosity in sublayer (Equation 18)
ν	Kinematic viscosity
ν_w	Kinematic viscosity at wall
Π	Wake parameter (Equation 24)
ρ	Density
ρ_r	Characteristic density in sublayer (Equation 18)
τ_i	Angles (degrees) surrounding a grid point. (Equation 5)
τ	Shear stress
τ_w	Shear stress at wall
ω	Vorticity
$ \omega_{max} $	Magnitude of maximum vorticity (mixing layer model) (Equation 16)
ξ	Computational axis (index - i)
ψ_k	Interpolants for multisurface technique (Equation 2)
ζ	Computational axis (index - k)

Subscripts

j	jet
t	total (temperature for example)
w	evaluated at wall
∞	Evaluated at freestream

END

DATE

FILMED

S-88

DTIC